AIP | Physics of Plasmas

Comparison of edge turbulence imaging at two different poloidal locations in the scrape-off layer of Alcator C-Mod

S. J. Zweben, J. L. Terry, M. Agostini, W. M. Davis, A. Diallo et al.

Citation: Phys. Plasmas **20**, 072503 (2013); doi: 10.1063/1.4813758
View online: http://dx.doi.org/10.1063/1.4813758
View Table of Contents: http://pop.aip.org/resource/1/PHPAEN/v20/i7
Published by the AIP Publishing LLC.

Comparison of edge turbulence imaging at two different poloidal locations in the scrape-off layer of Alcator C-Mod

S. J. Zweben,[1] J. L. Terry,[2] M. Agostini,[3] W. M. Davis,[1] A. Diallo,[1] R. A. Ellis,[1] T. Golfinopoulos,[2] O. Grulke,[4] J. W. Hughes,[2] B. LaBombard,[2] M. Landreman,[2] J. R. Myra,[5] D. C. Pace,[6] and D. P. Stotler[1]
[1]*Princeton Plasma Physics Laboratory, Princeton, New Jersey 08540, USA*
[2]*Massachusetts Institute of Technology, Cambridge, Massachusetts 02139, USA*
[3]*Consorzio RFX, Associazione Euratom-ENEA sulla fusione, C.so Stati Uniti 4, I-3512 Padova, Italy*
[4]*Max Planck Institute for Plasma Physics, EURATOM Association, D-17491 Greifswald, Germany*
[5]*Lodestar Research Corporation, 2400 Central Ave., Boulder, Colorado 80301, USA*
[6]*General Atomics, P.O. Box 85608, San Diego, California 92186-5608, USA*

(Received 30 March 2013; accepted 3 June 2013; published online 23 July 2013)

This paper describes 2D imaging measurements of plasma turbulence made in the scrape-off layer of the Alcator C-Mod tokamak simultaneously at two different poloidal locations, one near the outer midplane and the other near the divertor X-point region. These images were made with radial and poloidal resolution using two gas puff imaging diagnostics not directly connected along a B field line. The turbulence correlation structure has a significantly different tilt angle with respect to the local flux surfaces for the midplane and X-regions, and a slightly different ellipticity and size. The time-averaged turbulence velocities can be different in the midplane and X-regions, even within the same flux surface in the same shot. The structures are partially consistent with a magnetic flux tube mapping model, and the velocities are compared with various models for turbulence flow. © *2013 AIP Publishing LLC*. [http://dx.doi.org/10.1063/1.4813758]

I. INTRODUCTION

The general motivation for this paper is to better understand the plasma transport in the scrape off layer (SOL) of tokamaks. This is important since it partially determines the heat and particle deposition at the machine's divertor plates and first wall, and so will affect the engineering design of future tokamaks. The subject of plasma turbulence is also a challenging and fascinating topic in itself.

Turbulence in the edge of tokamaks is usually measured near the outer midplane where the edge turbulence level is large and diagnostic access is the easiest. However, since the theory and modeling of tokamak edge turbulence can now be done in 3D geometry, including the X-point and divertor regions, it is interesting to try to validate such theory with 3D measurements of the structure and motion of edge turbulence.

The present paper compares gas puff imaging (GPI) measurements made of edge turbulence at the outer midplane and X-point regions of Alcator C-Mod, as shown in Fig. 1. These measurements were made simultaneously with 2D radial vs. poloidal resolution in both regions, although these two regions were *not* directly connected along a single magnetic field line due to diagnostic location constraints. The results were mainly obtained for the SOL region outside the separatrix using standard C-Mod lower-single-null diverted discharges. For this paper the experimental results are compared with relatively simple theoretical models, since 3D turbulence simulations of these discharges are not yet available.

The 3D structure of SOL turbulence in tokamaks has been measured to a limited extent, as reviewed previously.[1,2] In general, edge density and electrostatic potential fluctuations have a long correlation length along the magnetic field lines (i.e., many meters), as seen, for example, in JET,[3] C-Mod,[4] and NSTX.[5] This is due to the rapid electron motion along the magnetic field B, which equilibrates the potential at the electron thermal or Alfvén speed. The turbulence structure perpendicular to B is always much smaller (i.e., centimeter-scale), often forming spatially isolated and intermittent structures in the SOL known as blobs. Thus, the 3D structure of SOL turbulence generally consists of filaments aligned along B with small-scale structures perpendicular to B. However, the parallel correlation along B is not perfect, and some parallel variation is expected theoretically,[6,7] for example, when the timescale for turbulent perpendicular $E \times B$ drifts across the SOL is less than the parallel ion transit time, or due to variations in the magnetic structure, plasma parameters, or fluid velocities along B. Thus, there may be significant poloidal variation in the structure of SOL turbulence.

Direct measurements of the poloidal variations in the SOL turbulence of diverted tokamaks were also reviewed in Refs. 1 and 2. The clearest poloidal variation observed so far for tokamaks is a large ($\times 10$) reduction in the turbulence level at the inner midplane (small major radius) compared with the outer midplane (large major radius), e.g., in Alcator C-Mod.[8] This is expected due to the difference in the interchange drive (ballooning), although no quantitative comparisons with theory have yet been made. Several measurements of turbulence have also been made using Langmuir probes in tokamak divertor regions. A higher relative level of ion saturation current fluctuations was observed at the outer divertor target plates compared to the inner target in JET, with the

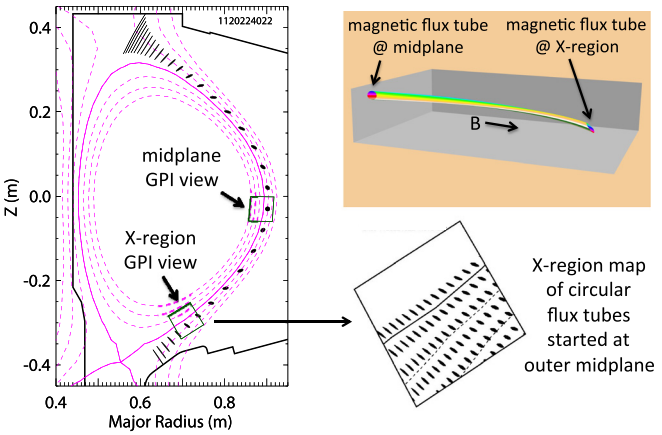

FIG. 1. Typical C-Mod plasma cross-section showing the locations of the midplane and X-region GPI views and nearby flux surfaces (#1120224022). Each GPI view is 5.9 cm × 5.9 cm and oriented in the local radial vs. poloidal (i.e., bi-normal) direction. The black shapes show the poloidal variation of an assumed circular magnetic flux tube at the outer midplane. At the right is a 3D visualization of a magnetic flux tube along the 1.7 m between the midplane view and the X-region view.

highest level in the private flux region.[9] A vertically scanning probe in the DIII-D divertor showed large relative fluctuation levels (~10%-100%) in potential (normalized to the electron temperature T_e) in the SOL and private flux region.[10] In MAST, the intermittency was high at the outboard (low field) divertor target plates, but low or absent around the X-point and high-field target plates.[11] In NSTX the turbulence at the divertor plate surfaces was measured using LiI line emission and showed an interesting pattern of toroidal vs. radial filamentation, which was correlated by field-line mapping to the midplane blob structures seen by GPI.[5]

Initial GPI measurements of edge turbulence near the lower X-point region of C-Mod[12] showed unusually elongated 2D turbulence structures compared with the nearly isotropic structures normally seen at the outer midplane.[8] This X-region structure was interpreted in terms of a magnetic flux tube model in which an assumed circular blob at the outer midplane was mapped along a flux tube to the GPI view at the X-region. The present paper uses the same X-region GPI view, but now directly compares the X-region and outer midplane turbulence measured at the same time (but not along the same field line), and also uses a wider C-Mod database and an improved GPI diagnostic. The present paper also compares the time-averaged turbulence flow velocity at the outer midplane and X-point regions using these same two GPI views. The edge turbulence velocity in C-Mod was previously measured using GPI,[12–14] but not in both regions simultaneously. Recent Langmuir probe measurements of turbulent transport in the SOL of C-Mod have also shown that the fluctuation-induced radial particle flux on the high field side midplane location much lower than at the low-field side midplane.[15]

In other tokamak devices, the most closely related recent work was done at Tore Supra, where the relationship between the turbulence structure, velocity, magnetic, and electric field shear was analyzed for the SOL.[16] Turbulence measurements by probes at the top of Tore Supra were consistent with a model in which the turbulence was transported across the separatrix near the outer midplane, and propagated along B field lines to the top. Recent results from a dual GPI diagnostic on the EAST tokamak have also shown that the SOL turbulence structure and velocity were different ±50° above and below the outer midplane.[16,17]

The outline of this paper is as follows: Sec. II describes some theoretical background relevant for this experiment, Sec. III describes the GPI diagnostic and data analysis procedures, Sec. IV describes the experimental results, and Sec. V contains the discussion, summary, and conclusions.

II. THEORETICAL BACKGROUND

The basic theoretical issues relevant to this experiment concern the 3D structure and motion of turbulence in the SOL of a diverted tokamak. In this paper "turbulence" refers to electrostatic fluctuations and not to turbulent magnetic field fluctuations, which are usually small in the SOL (except perhaps during edge localized modes (ELMs)), and were not measured in this experiment. Because of the rapid electron motion along B, the structure of the electrostatic potential is believed to have a parallel wavelength much longer than the perpendicular wavelength, but it is not clear whether the 3D structure is flute-like (with $k_{||} = 0$) or drift-ballooning-like ($k_{||} \sim 1/qR$), or whether some other scales may be involved. Analytic calculations in tokamak geometry showed clearly that the shape of a magnetic flux tube changes significantly as a function of poloidal angle in the SOL due to magnetic shear and flux expansion,[18] which suggests that the turbulence structure should vary with poloidal angle.

An illustration of this magnetic flux tube variation is shown in Fig. 1 for a typical discharge in this experiment. The black filled shapes in the plot at the left shows how a 1 cm diameter circular flux tube started at 1 cm outside the separatrix at the outer midplane is distorted in shape and tilted as a function of the poloidal angle. By the time this flux tube reaches the X-region GPI view it is elongated by a factor of ~3 due to the flux expansion between these two regions, since the innermost and outermost radii of the flux tube remain the same in flux surface coordinates. Since the area of a flux tube depends inversely on B, it should decrease by a factor of ~0.8 from the outer midplane to the X-region view, and so the minimum width of the flux tube decreases by somewhat more than a factor of 3. The tilt angle of these flux tubes depends on the local magnetic shear, which depends on the plasma shape. The ellipticity and tilt of these flux tubes vary slowly over the X-region field of view, as shown in the map of X-region flux tubes at the lower right, all of which were mapped from 1 cm diameter circles at the outer midplane.

The theory of SOL turbulence in tokamak geometry has been developed both from first principles, using computational solutions of the basic equations, and also from simplified analytic models assuming relatively isolated blob-filaments. The radial and poloidal motion of isolated plasma blob-filaments in the SOL was calculated by Ryutov to depend on the poloidal location of the filament,[19] which was assumed to extend only part of its length along the field line

length in the SOL. The motion of the blob-filament was also shown to depend on its degree of connection with the divertor plate, which affects the electrostatic potential in the filament. The local acceleration acting on a segment of an ideal blob-filament is in the $-\nabla B$ direction.[19] These filaments can become disconnected from the divertor plate due to the narrowness of flux tubes near the X-point, or by a high electrical resistivity in the SOL.[6] The motion of blob-filaments can also be modified by drift wave formation in the SOL,[7,20] and can interact with the parallel dynamics and transport.[6,21]

The effects of electric fields and electric field shear on the motion and structure of blobs have been addressed in model simulation studies. In a homogeneous background plasma, blobs convect with the local $E \times B$ drift velocity. If the $E \times B$ velocity is sheared, it will shear and possibly tear apart the blob structure.[22] The motion of the centroid of a blob is also affected by a velocity shear layer which can act to accelerate or decelerate it depending on the relative signs of vorticity of the shear layer and the blob.[23] Inhomogeneities in the background plasma modify both the blob motion and the structure.[23,24] Finally, in the presence of toroidal rotation the blob-filaments, which have a density approximately constant along helical field lines, can acquire apparent poloidal motion when viewed at a fixed toroidal angle (the "barber pole" effect).

In the area of computational simulations of edge turbulence, linear stability calculations have been done for 3D tokamak geometry which show a variety of unstable ballooning modes and drift waves in the SOL. In the fluid limit the SOL stability depends on dimensionless parameters such as R/L_n, β, parallel resistivity, the magnetic shear, and the assumed flux surface geometry and boundary conditions. The latter has varied from a realistically shaped diverter model with sheath boundary conditions[25] to a simplified circular limited model.[26] Not yet included in these models are kinetic effects, sheath instability effects, or atomic physics, which all could play a role in the SOL linear stability. Since the linear growth phase lasts only a fraction of a millisecond, and since experiments have shown that the SOL is normally turbulent, linear stability calculations are not considered to be relevant for comparison with experiments.

The nonlinear theory of edge turbulence is complicated,[27] but simplified 2D turbulence models with assumed parallel boundary conditions have been developed and compared with outer midplane measurements.[28,29] However, a full 3D geometry is needed to understand the poloidal dependence of the turbulence. The 3D edge turbulence was modeled in the BOUT fluid code, and initial comparisons were made with the structure of the turbulence in the C-Mod midplane[30] and X-point region.[12] The 3D GEM-R gyrofluid code was compared with the midplane C-Mod GPI data,[31] but not with C-Mod X-region data. SOL turbulence was modeled with the GBS code in a simplified toroidal geometry, and initial comparisons were made with TORPEX measurements.[32] Recently the BOUT code was used to calculate the edge and SOL turbulence in DIII-D, and the results appeared to agree well with midplane probe and BES measurements of turbulence.[33]

III. GPI DIAGNOSTIC AND DATA ANALYSIS

This section describes the GPI diagnostic and data analysis used for this experiment. Sections III A and III B describe the hardware, Secs. III C and III D describe the diagnostic operation and database, and Secs. III E and III F describe the data analysis. Some of the limitations and uncertainties in the diagnostic and data analysis are described in Sec. III G.

A. GPI overview and geometry

The gas puff imaging diagnostic has been used previously on Alcator C-Mod,[8,12–14] NSTX,[34] RFX-Mod,[35] Gamma-10,[36] Heliotron J,[37] TEXTOR,[38] and EAST.[16,17] A localized neutral gas puff of D_2 or He is introduced near the vessel wall and viewed along the direction of the local magnetic field line using a fast camera. The neutral atom light emission in D_α (651 nm) or HeI (587 nm) is resolved in the 2D radial vs. poloidal (i.e., binormal) plane on a spatial scale of a few millimeters and a timescale of a few microseconds. This light emission is limited to the region where $T_e \sim 10$–100 eV where these atoms are neutral, so the GPI can see only the edge and SOL region of most tokamaks.

Since the neutral light emission is proportional to the local electron excitation, the space-time fluctuations of the light emission are interpreted in terms of the local electron density/temperature fluctuations. The space and time cross-correlation functions are largely insensitive to the nonlinearity between the underlying plasma density and/or temperature fluctuations and the neutral light emission.[34,39] The time-averaged 2D profiles of neutral line emission have been successfully compared with calculations based on the measured edge temperature and density profiles and the neutral and atomic physics in the DEGAS 2 simulation, both for He in C-Mod[40] and D in NSTX.[41] The time response of the HeI line to fluctuations should be $\leq 1\ \mu$s for SOL plasmas.[40]

Figure 1 shows a cross-section of an Alcator C-Mod plasma in the (R,z) plane along with the location of the two GPI viewing regions and sample magnetic flux surfaces. The plasmas have major radius of $R = 67$ cm, a minor radius of $a = 23$ cm, and a standard lower single-null divertor shape with an elongation of typically $\kappa = 1.6$. The "midplane" GPI camera view is centered 3 cm below the outboard midplane, and the "X-region" GPI camera view is centered 30 cm below the midplane near (but not overlapping with) the divertor X-point. Both viewing regions are approximately square and extend ~5.9 cm radially and ~5.9 cm poloidally, covering the separatrix (solid line) and flux surfaces up to about $\rho = 2$ cm outside the separatrix (dashed lines), where ρ is the radial distance outside the separatrix measured at the outer midplane. Note that the actual GPI optical sightlines are aligned along the local direction of the total magnetic field at these two locations (see Sec. III B), so the regions shown in Fig. 1 are the projections of these views in the (R,z) plane.

The black circle shown at the outer the midplane in Fig. 1 is the cross-section of an assumed circular magnetic flux tube at $\rho = 1$ cm outside the separatrix, and the other black shapes show how this flux tube is elongated and tilted

as it follows the magnetic field line to different poloidal locations. These shapes show the intersection of flux tubes with planes of constant toroidal angle, which are very similar to the cross-sections perpendicular to B. This flux tube distortion occurs both above and below the midplane, so does not require the presence of an X-point. Similar looking flux tubes are obtained over all radii in the SOL of C-Mod (see Fig. 1 and Ref. 12), and a similar-looking flux-tube distortion was calculated for the circular limited Tore Supra.[16] A 3D visualization of the magnetic flux tube between these two poloidal locations is also shown at the upper right in Fig. 1.

Due to internal vessel constraints, these two GPI views were *not* designed so as to view the same magnetic field line in the SOL. Thus the comparisons between the midplane and the X-region turbulence are not based on direct cross-correlations between them, but on statistical differences in the turbulence structure and velocity between them. The specific location of these two views with respect to magnetic field line mappings is discussed in the Appendix.

B. GPI diagnostic hardware

The optical hardware for the *midplane* GPI view is the same as described previously.[13] An in-vessel telescope was mounted on the outer wall and pointed at the center of the midplane view of Fig. 1 in the local B field direction, which was 11° below horizontal, as determined from typical EFIT equilibria. A vertically distributed four-hole gas puffer was located just outside the midplane viewing region of Fig. 1. The images were transmitted to a Phantom 710 camera using a 57 × 57 pixel coherent quartz fiber optic bundle inside a long bellows. The spatial resolution of the whole optical system was ~2-3 mm for objects in the midplane view.

Initial results from the X-region view were described briefly,[12] so more details of the hardware are described here. A second in-vessel telescope was mounted on the outer wall and pointed at the center of the X-region view of Fig. 1 in the local B field direction, which was 4° below horizontal, as determined from typical EFIT equilibria. This telescope was 43° toroidally from the center of the X-region gas puff at a distance of 0.73 m. A design study showed that variations in the local B field angle over the X-region view were ±1° over a ±3 cm variation in R, and ±1.5° over a ±3 cm variation in z; thus, the local B field direction varied by only about ±2° over this field of view. The gas puff nozzle for this view was a single-hole capillary tube located in a divertor-target tile at the wall ~3 cm below the bottom of the X-region view.[12] The helium gas to this view was triggered independently from the midplane GPI gas puff. The telescope optics, fiber optic bundle, and camera for the X-region view were similar to the midplane view, and the spatial resolution of the whole optical system was also ~2–3 mm.

The main difficulty with the X-region view was the relatively large background light from the lower divertor region behind the X-region view. The best solution to this problem was to use helium gas in the GPI (with deuterium plasmas), as was done in the present experiment, although some deuterium GPI results were obtained with double-null deuterium discharges, as reported previously.[12] Another problem was breakage of the insulating section of the capillary tube which was needed to electrically isolate the X-region GPI gas nozzle; this was solved by using a commercial alumina-to-stainless isolator (CeramTec). The X-region nozzle was put as close as possible to the X-region GPI view, but this distance (~3 cm) was farther than the distance from the midplane nozzle to the edge of the midplane view (~0.1 cm).

C. GPI diagnostic operation

All data in this paper were taken using helium GPI puffs viewed with He I (587.6 nm) line filters. A total of 6–8 Torr-liters (~2–3 × 10^{20} atoms) was puffed over ~200–300 ms for each shot, about half going to each GPI view. The two Phantom 710 cameras were always operated at 391 000 frames/s with a frame separation time of ~2.6 μs, an exposure time of ~2.1 μs/frame, with a 64 × 64 pixel format for this experiment. Since the majority gas was deuterium in all cases, the GPI HeI signal was nearly zero in both views before the puff. These GPI signals rose with the puff over ~30 ms, and stayed fairly constant for the next ~50–100 ms. Camera data were acquired for 60 000 frames/shot over ~150 ms (~0.4 GB per camera per shot).

Figure 2 shows typical single frames of the (normalized) GPI light signals for the X-region view (left) and midplane view (right), taken at the same time in the same shot with a camera exposure of ~2.1 μs. Also shown are the separatrix locations (solid line) and SOL flux surfaces at $\rho = 1$ cm and 2 cm (dashed lines), taken from EFIT equilibria. The false-color scale of Fig. 2 ranges from 0.5 (black) to 1.5 (white), where each pixel has been normalized by its time average over ~4 ms, and the pixels with low average signal levels (≤25 counts) are shown as black. Un-normalized signal levels near $\rho = 1$ cm are typically ~100–200 counts in the midplane and ~50–100 counts in the X-region, and useful GPI data in these experiments typically covered the radial region from ~0.5 cm inside the separatrix to ~2 cm outside the

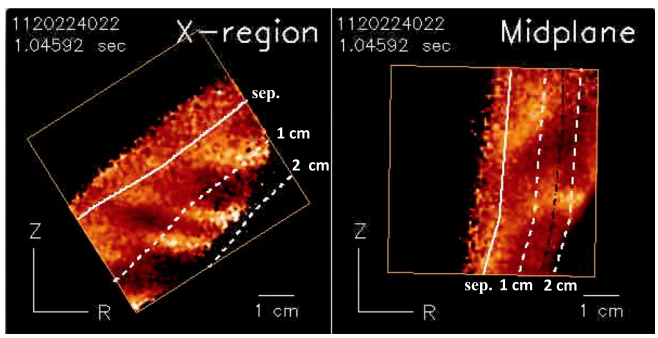

FIG. 2. Typical images of a single frame from the X-region camera (left) and the midplane camera (right), taken at the same time. The data were all normalized by the time-averaged of the images over 4 ms, and displayed in a false-color scale from 0.5 (black) to 1.5 (white), with low-signal-level pixels set to black. The separatrix at $\rho = 0$ cm and SOL flux surfaces at $\rho = 1$ cm and 2 cm are shown by solid and dashed lines, respectively, and the limiter shadow is shown by the black line in the midplane view. The turbulence structures tend to be elongated in the major radial direction in the X-region and more circular in the midplane region (enhanced online) [URL: http://dx.doi.org/10.1063/1.4813758.1] [URL: http://dx.doi.org/10.1063/1.4813758.2] [URL: http://dx.doi.org/10.1063/1.4813758.3] [URL: http://dx.doi.org/10.1063/1.4813758.4].

TABLE I. Shot list.

Shot	Time (s)	I (MA)	B (T)	n (m^{-3})	RF (MW)	Gap[a] (cm)	Discharge type
Run #1							
1120224009	0.701–0.716	0.9	4.6	1.1×10^{20}	2.3	1.3	L-mode
1120224015	0.810–0.814	1.0	6.0	1.3×10^{20}	3.7	1.1	L-mode
1120224022	1.044–1.048	1.0	5.2	1.0×10^{20}	2.6	1.2	L-mode
1120224023	1.113–1.116	1.0	5.2	1.4×10^{20}	3.0	1.3	ELM-free H-mode
1120224024	1.130–1.135	1.0	5.2	1.7×10^{20}	2.8	1.5	ELM-free H-mode
1120224027	1.144–1.148	0.9	4.6	1.3×10^{20}	3.0	1.4	L-mode
Run #2							
1120712026	1.440–1.444	0.73	4.2	3.5×10^{20}	0	0.2	Ohmic H-mode
1120712027	1.440–1.444	0.73	4.2	3.6×10^{20}	0	0.1	Ohmic H-mode
1120712028	1.440–1.443	0.73	5.0	2.6×10^{20}	0	0.1	Ohmic H-mode
1120712029	1.440–1.443	0.73	5.0	2.2×10^{20}	0	0.1	Ohmic H-mode
Run #3							
1120815018	1.270–1.274	0.90	5.6	2.5×10^{20}	2.9	1.4	ELMy H-mode
1120815021	1.190–1.193	0.91	5.6	2.0×10^{20}	2.0	1.4	ELMy H-mode
1120815030	1.260–1.264	0.91	5.6	1.9×10^{20}	2.6	1.5	ELMy H-mode
1120815034	1.150–1.153	0.91	5.6	2.0×10^{20}	3.1	1.7	ELMy H-mode

[a]Outer gap distance between outer midplane separatrix and innermost outer limiter.

separatrix. The radial range of useful GPI data varied with the location of the separatrix with respect to the gas nozzles, but a typical case is illustrated in Fig. 2. The inner edge of the shadow of the innermost outboard limiter (located at a different toroidal angle than the GPI) is shown by the black line in the midplane view, and cross-sections of the divertor plates at the focal plane of the X-region view are outside its view (the divertor target plates behind the gas puff in this downward-pointed X-region view are viewed out-of-focus).

Note that since the optical sightlines are aligned (nearly) along the local direction of the total B at these two locations, the images in Fig. 2 show the turbulence in the plane perpendicular to B, i.e., in the radial vs. poloidal (i.e., binormal) direction. Therefore in this paper the word "poloidal" refers to the direction perpendicular to the total B and also perpendicular to the radial direction across magnetic flux surfaces.

D. Database and overview of data

The database of shots used in this experiment is shown in Table I. All shots are deuterium fueled, lower-single-null diverted discharges, and were done during three different days in 2012 (runs #1-3 in Table I). The times of interest for the GPI analysis were chosen during steady-state periods to avoid transient events such as L-H transitions, ELMs, and variations in RF heating. The range of plasma parameters was toroidal field $B_o = 4.2–6.0\,T$, plasma current $I = 0.73–1.0$ MA, $q_{95} = 3.3–5.0$, and line-averaged density $n = 1.0–3.6 \times 10^{20}\ m^{-3}$, all of which are within the normal range of C-Mod operation. These densities spanned a range of values normalized to the Greenwald density of $\sim 0.2 n_G$ (run #1), $\sim 0.5–0.8 n_G$ (run #2), and $\sim 0.5 n_G$ (run #3).

Typical SOL plasma parameters for the first and third run days are summarized in Table II, which are also in the normal range for C-Mod.[42] The first run consisted of RF-heated discharges at low-to-moderate density. Some data were taken in L-mode close to the L-H transition, and others in a brief ELM-free H-mode. Cases examined in run #2 consist of Ohmic EDA H-modes initiated by toroidal field ramps. Some of the Ohmic H-modes had short-wavelength magnetic perturbations injected at the edge by a "shoelace" antenna, although these perturbations are not thought to have substantially affected the edge turbulence. The third run examined RF-heated ELMy H-modes.[43] There were at least two different RF antennas active for the first and third run days. The equilibria were slightly different for each run, e.g., the "outer gap" (the distance between the separatrix and the outer midplane limiter) was $\sim 1.1–1.7$ cm for the RF runs #1 and #3, but only ~ 0.1 cm for Ohmic run #2. In the Ohmic run, the SOL was relatively narrow and the field lines outside $\rho \sim 0.5–1.0$ cm were intercepted by limiters before they reached the divertor plates. However, in all cases both GPI systems had good signal levels out to at least $\rho \sim 2$ cm into the SOL.

Sample movies of the normalized turbulence images in the same format as Fig. 2 are located in the "Integral Multimedia" for this paper, and also on a public web site at

TABLE II. Typical SOL parameters.

Parameter	Run #1	Run #3
Regime	L-mode	H-mode
ρ at midplane (cm)	0.5 ± 0.5	0.5 ± 0.5
n_e ($10^{19}\ m^{-3}$)	3.1 ± 1.1	4.9 ± 0.6
T_e (eV)	21 ± 5	18 ± 2
L_n (cm)	1.1	1.2
L_{Te} (cm)	0.6	0.5
$L_{\parallel,min}$ (m)[a]	~ 4	~ 8
ρ_s (cm)	$\sim 10^{-2}$	$\sim 10^{-2}$
$\Lambda = \nu_{e*}\,(m_e/m_i)^{1/2}$	0.4	1.6
β	$\sim 3 \times 10^{-5}$	$\sim 3 \times 10^{-5}$

[a]Distance from outer midplane to divertor plate along B.

Ref. 44. These movies show a complex turbulent structure and motion in both the midplane and X-region views. The turbulence structures have a typical size scale of ~1 cm in both views, but the shapes appear more elongated in the major radial direction in the X-region view compared with the midplane view. The turbulence motion does *not* look like a "frozen flow" on space-time scale of these images, but the turbulence usually moves at least one correlation length before changing shape, similar to clouds moving across the sky. There is sometimes a relatively uniform poloidal drift velocity of the turbulence over each these views (e.g., in the X-region of 1120224009), but normally the poloidal velocity varies as a function of radius and time. There is no clear correlation visible by eye between the poloidal turbulence motion in the two views (as discussed quantitatively in Sec. IV). The radial component of the turbulence velocity is generally smaller than the poloidal component, except for the Ohmic plasmas in which it can be dominant, and a radially outward motion is much more common than an inward radial motion. There is no immediate (i.e., sub-millisecond) change in the turbulence structure or velocity with the turn-on or turn-off of RF heating, but there are complex variations during ELMs and L-H transitions, which are not treated in the present paper.

E. Turbulence structure analysis

The structure of the turbulence was analyzed by first normalizing (i.e., dividing) each 64 × 64 pixel frame by the time-averaged frame for that shot over 3–5 ms (1200–2000 frames), and then smoothing the results for each frame over 3 pixels in space (~0.3 cm) to reduce the random noise level. Only regions with relatively large signal level were used, which limited the analysis to between ~0.5 cm inside the separatrix to ~2 cm outside the separatrix. After normalization, the cross-correlation coefficient between any chosen pixel and all other pixels in the image was calculated by averaging over the time of interest. Starting from the chosen point where the cross-correlation was 1.0, one dimensional cross-correlation functions were then calculated for each rotation angle in the image plane (in 1° increments). For each rotation angle, the length over which the correlation coefficient was ≥0.7 was evaluated in order to find the shape of the highly correlated part of the turbulence structure. The maximum and minimum of these lengths for any rotation angle were used to characterize the turbulence size at that pixel location. The angle of the maximum length was used to characterize the turbulence tilt angle, and the ratio of the maximum length to the length at 90° to this maximum was used to characterize the turbulence ellipticity (a similar analysis of X-region images was done in Ref. 12). The results of this analysis are in Sec. IV B.

A separate analysis of the tilt angle and ellipticity was done using discrete blob structures, similar to that done previously for NSTX GPI data.[23] The images were first normalized and smoothed as above. Then resulting images were contoured at 1% intervals, and the closed contours which fit certain assumed size constraints were considered to be blobs. The contour midway between the lowest and highest level contours was fit with an ellipse. The ellipticity, size, tilt angle, height, and location of the peak of these blobs were recorded for each frame. The blobs were tracked from frame-to-frame given certain constrains such as a maximum displacement of 10 pixels per frame, corresponding to a maximum speed ≤3.2 km/s, and blob speeds and lifetimes were then recorded. The results from the blob analysis are similar to the cross-correlation analysis.

F. Turbulence velocity analysis

The time-averaged turbulence velocity was evaluated at any given pixel by first normalizing and smoothing the images as above, and then evaluating the time-delayed cross-correlation coefficient from that pixel using ±8 adjacent pixels in either direction (i.e., ±0.7 cm) for time delays of up to ±10 frames (i.e., ±25 μs). For each time delay the 2D velocity was evaluated as the 2D distance to the pixel of maximum cross-correlation divided by that time delay, and the velocity for that pixel was the average over all the time delays which had a cross-correlation coefficient above 0.5 (but only if there were at least four time such time delays). This process only finds local velocities within the range ±2.8 km/s in either direction, but essentially all velocities found this way were well within this range (i.e., ≤1.5 km/s). These velocities were sometimes averaged over 0.5 cm wide radial zones using every third pixel in either direction, as described in Sec. IV C. These averages were very similar when using every pixel or every third pixel.

G. Limitations and uncertainties

This GPI diagnostic and data analysis have many limitations and uncertainties. First of all, this diagnostic measures only HeI neutral light, which can respond to both electron density and temperature fluctuations.[39,40] Thus, the relative fluctuation level in the GPI signal is not simply proportional to the density fluctuation level. If the electron density and temperature fluctuations are different from each other, the GPI will measure some complicated mixture of the two; thus, we tentatively assume that electron temperature and density fluctuations are well correlated in both regions (see Sec. V D). We also assume that the He neutral density is not fluctuating on the space-time scale of the turbulence, although there could be some shadowing effect due to the turbulence itself.[39] There is evidence that the GPI turbulence signals in the SOL are at least partially correlated to Langmuir probe turbulence signals when measured on the same field line, for example, in C-Mod,[4] NSTX,[45] and TPE-RX.[46]

The analysis of the turbulence structure as described in Sec. III E assumes that the GPI telescope is viewing exactly along the local B field at the gas cloud. The actual field line angles (according to EFIT) in this experiment were 8.5°–12° below the toroidal direction for the midplane view, and 3.5°–5° below the toroidal direction for the X-region view, which are within ~2° of the telescope sightlines of 11° and 4°, respectively. The degradation of the spatial resolution of the GPI images depends on the misalignment angle and the length of the sightline through the GPI gas cloud. A

simulation of the toroidal extent of the GPI gas cloud using DEGAS 2 gave a cloud FWHM of ~6 cm for the midplane view,[31] and a separate simulation of the X-region GPI view gives a toroidal extent of ~4 cm at the bottom (low-z) edge of the view, 8 cm at the center, and ~11 cm at the top (these results are nearly the same for deuterium and helium). Therefore these misalignments should result in a point-source spread of ≤0.3 cm in these images, which is comparable to the spatial resolution of the diagnostic, and so should have a relatively small effect on the size and orientation of the ~1 cm turbulence structures in this experiment. As described in Ref. 12, if the gas cloud somehow had a toroidal extent of 20 cm FWHM, it would result in measured elongations that are longer and tilts that are significantly more horizontal than the actual cross-sections of structures in a single toroidal plane.

The analysis of the turbulence velocity described in of Sec. III F has several important limitations, most of which have been discussed previously.[47] This method cannot detect flows along the direction of constant GPI intensity, or resolve separately counter-propagating flows, and cannot measure the phase velocity of these perturbations. This particular cross-correlation method detects only velocities ≤2.8 km/s, which can miss some faster moving flows in the far-SOL that exist during RF heating,[14] or faster flows near or inside the separatrix. However, this method does correctly track the 2D velocity of small-scale features, similar to the way the wind speed can be inferred from moving clouds. This turbulence velocity is *not* necessarily the same as the E × B fluid (ion) flow velocity, since there also may be turbulence propagation in the rest frame of the plasma (see Sec. V B).

Some other limitations of the cross-correlation method for velocity analysis have been described recently.[16,48,49] There are fundamental ambiguities in velocity estimates made using 1D cross-correlations in a 2D velocity field; however, the method of Sec. III F uses a 2D cross-correlation analysis, so should be relatively immune to these difficulties, subject to the limitations discussed in Ref. 47. There can also be significant sources of noise in the time-dependent evaluation of turbulent velocity, e.g., for estimating zonal flows; however, velocity fluctuations are not the main focus of the present paper.

The separatrix and SOL flux surface locations were calculated using EFIT equilibrium reconstructions and not directly measured in these experiments. Recent analysis of C-Mod probe data[15] indicated that flux surface shifts of ~0.1–0.5 cm were required to match the horizontal probe data just above the outer midplane, and ~0.1 cm shifts were required to match the vertical probe near the X-region GPI poloidal location. For displaying radial profiles, the GPI data were binned in 0.5 cm radial zones in this experiment.

A general uncertainty in this paper is whether the GPI gas puff can significantly perturb the local plasma or turbulence as measured by the GPI. It is difficult to resolve this uncertainty directly, since there were no other SOL measurements in C-Mod at the same place and time as the GPI. Although there was a high correlation between the turbulence seen by GPI and a Langmuir probe located on nearly the same B field line,[4] this does not exclude the possibility that one or both of these diagnostics were perturbing the turbulence. Since there were two helium puffs in these experiments, there was a sometimes relatively large increase in the line-averaged density of up to 10%–20% due to these puffs. However, such density changes are comparable to the shot-to-shot variation in this experiment and do not imply any unusual perturbation of the edge turbulence. There were no systematic changes in the turbulence seen in the GPI as a function of time during the puff, indicating that the observed turbulence did not depend on the rate of gas influx. There were no systematic changes in global parameters such as the stored energy, radiated power, loop voltage or MHD activity due to these puffs.

A rough estimate of the perturbing effect of the GPI puff can be made based on the energy and particle flow into the magnetic flux tubes containing this puff, since the plasma parameters and turbulence are presumably determined by B-field line averages. The source rate of helium from the midplane GPI gas puff is $\sim 10^{21}$ neutrals/s over a poloidal length ~6 cm at the outer midplane separatrix, while the plasma heat and particle flux most likely occur over a poloidal length of roughly ~60 cm at the outboard separatrix. The expected radiation loss for a helium atom is ~100 eV/atom, and the energy needed to heat the neutrals to the SOL temperature is ~30 eV/atom. Thus the energy loss due to the puff is ~10–20 kW, while the plasma energy loss across the poloidal range of the puff is at least ~10% of the total heating power, i.e., ≥100 kW; therefore, the radiative cooling effect of the puff on the field line should be small. The plasma ion loss across the poloidal range of the puff is harder to estimate but is probably $\sim 10^{21}$ ions/s, which is comparable to the helium puff rate. Thus these puffs might well perturb the density on the local SOL field line, although measurements of this were not available on C-Mod. The neutral density in the GPI viewing region is certainly increased by the puff, but large neutral density perturbations in the edge of C-Mod are common due to limiters and RF heating, particularly near the divertor region. Since the sensitivity of the SOL turbulence to plasma or neutral perturbations is basically unknown, there is still some uncertainty about the effects of the GPI puff on the turbulence measured in this experiment.

IV. EXPERIMENTAL RESULTS

This section uses the analysis methods of Sec. III applied to the database of Table I. Section IV A compares the basic characteristics of the turbulence in the midplane and X-region views. Section IV B compares the 2D (radial vs. poloidal) spatial structure of the turbulence in these two views, Sec. IV C compares the time-averaged 2D velocity of the turbulence, and Sec. IV D summarizes some additional analysis of these data.

Note again that these two GPI views were *not* designed so as to view the same magnetic field line in the SOL, and there was almost never any significant cross-correlation between the turbulence seen in these two views (see Appendix). Thus, the comparisons between the midplane and the X-region turbulence described below are based on

statistical differences in the average turbulence structure and velocity between them.

A. Basic turbulence characteristics

Figure 3 shows some comparisons between the turbulence seen in the X-region and midplane GPI views for three typical shots, one from each of the run days of Table I. The horizontal coordinate is the radial distance ρ outside the separatrix, as measured at the outer midplane (positive into the SOL). At the top are radial profiles of the relative GPI fluctuation levels (standard deviation/mean), averaged over radial flux surface zones of 0.5 cm width, and in the middle are the autocorrelation times (FWHM), averaged over the same regions. At the bottom are the frequency spectra (FFT amplitude) averaged over smaller regions near the center of the images at $\rho = 1$ cm. The data for each shot were time averaged over 3–5 ms during the steady-state part of these discharges in the absence of transient events. The low frequency peak in the midplane signal for 1120224022 at ~4 kHz is due the edge coherent mode mentioned in Sec. IV D.

The relative fluctuation levels are all fairly large (~10%–40%), the autocorrelation times are all relatively short (~10–50 μs), and the frequency spectra are all relatively broad (~1–100 kHz), all similar to those seen previously in the midplane GPI in C-Mod[8,12–14] and in the SOL of other tokamaks.[1,2] There is a possible trend for a larger autocorrelation time in the X-region compared with the midplane region. The probability distribution functions of the signal amplitude are near Gaussian in these cases, but have stronger positive skewness outside $\rho = 2$ cm, as seen previously on C-Mod and elsewhere. Thus, the basic turbulence characteristics were roughly similar in the outer midplane and X-region as seen in the GPI data.

B. Turbulence structure

Figure 4 shows typical 2D spatial cross-correlation functions calculated for the midplane and X-region views with zero-time delay, and plotted in the same format as for the

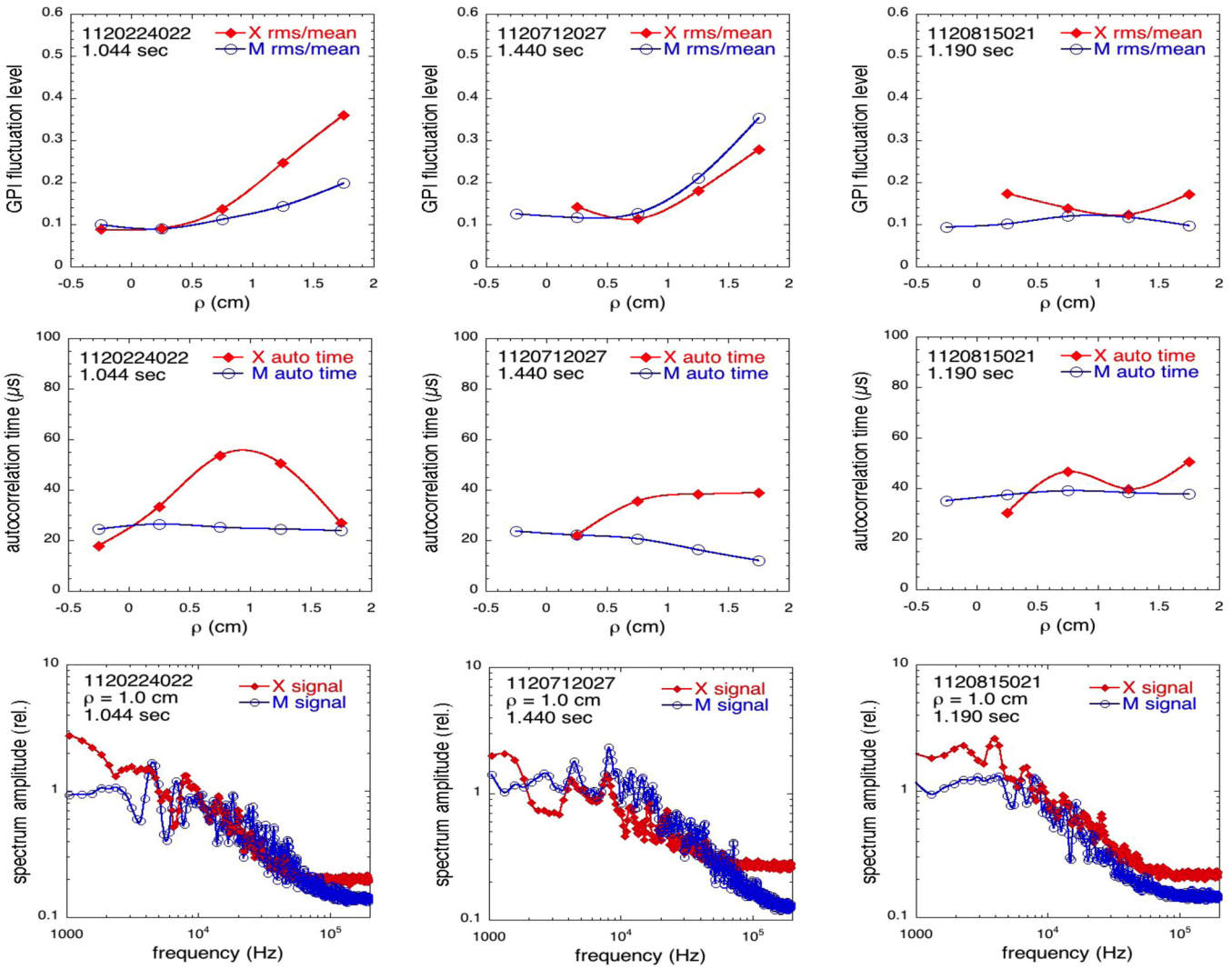

FIG. 3. Comparison of basic turbulence characteristics in the midplane and X-region GPI views for three typical shots, one from each of the run days of Table I. At the top are radial profiles of the relative GPI fluctuation levels (standard deviation/mean), in the middle are the autocorrelation times (FWHM), and at the bottom are the frequency spectra (FFT amplitude) averaged over regions near the center of the images at $\rho = 1$ cm. The basic turbulence characteristics were similar in the outer midplane and X-region GPI data.

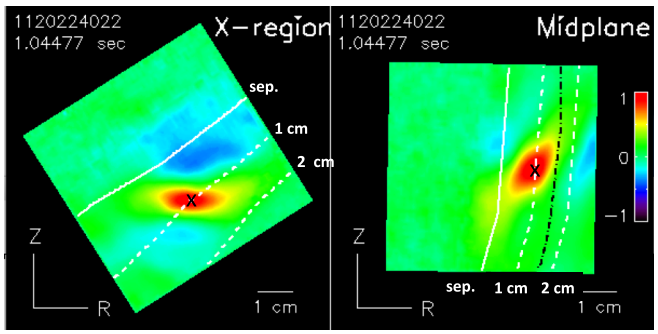

FIG. 4. Typical 2D spatial cross-correlation functions for the X-region (left) and midplane view (right), calculated from the central points marked with an "x," and averaged over 3 ms in time. This color scale has red near 1.0 (i.e., perfect cross-correlation), green near 0, blue near −0.5, and black at −1.0. The size and shapes of the correlation functions are roughly the same size in both regions, but they are tilted at different angles with respect to the (R,z) plane.

raw data in Fig. 2. These cross-correlation functions are calculated from the two points shown by the black "x" marks, which were both at a radius $\rho = 1$ cm in the SOL. The color scale in Fig. 4 follows the color bar at the right. The raw data were smoothed over ~0.3 cm before cross-correlation and time-averaged over 3 ms (1200 frames).

The cross-correlation function for the outer midplane in Fig. 4 has a size of ~0.5–1.5 cm FWHM, similar to that described previously for GPI in C-Mod.[8,12,13] The X-region cross-correlation appears elongated horizontally, i.e., in the major radius direction, similar to the initial deuterium GPI results for double-null discharges in this view.[12] There were often regions of negative cross-correlation about 1 cm radially inside or outside the peak correlation in both views, such as shown in blue in Fig. 4, but these are not universal in this dataset.

Figure 5 shows examples of 2D shapes of such cross-correlation functions over the X-region (left) and midplane (right) views for four typical shots (see the movies in "Integral Multimedia"). These maps are drawn for the same regions as Figs. 2 and 4 and oriented in the same direction. For both maps, the separatrix is shown by the solid line and flux surfaces in the SOL are shown by the dashed lines at 0.5 cm radial intervals out to $\rho = 2$ cm. The elliptical structures are defined by the shape and tilt direction of the 2D correlation functions at a correlation of 0.7, averaged over the time intervals in Table I (see Sec. III E). The size of these ellipses in Fig. 5 is reduced by a factor of three with respect to the images so that the ellipses do not overlap. In general, the correlation shapes in the X-region are more oriented in the major radius direction have higher ellipticity than those in the midplane region, although there are significant variations in shape and direction, particularly near or inside the separatrix and outside $\rho = 2$ cm.

Figure 6 shows a comparison between the turbulence correlation lengths and areas in the midplane and X-region, with one point per shot sorted in color according to run day. These lengths are based on data like that in Fig. 5 averaged over central regions of each view near $\rho = 1$ cm, as shown by the gray areas in Fig. 5 (±0.6 cm for runs #1 and #3 and ±0.3 cm for run #2). At the left are the maximum lengths of the correlation function in any direction within the 2D image plane, which were similar between the midplane and X-regions (~1–2 cm). In the middle are the minimum

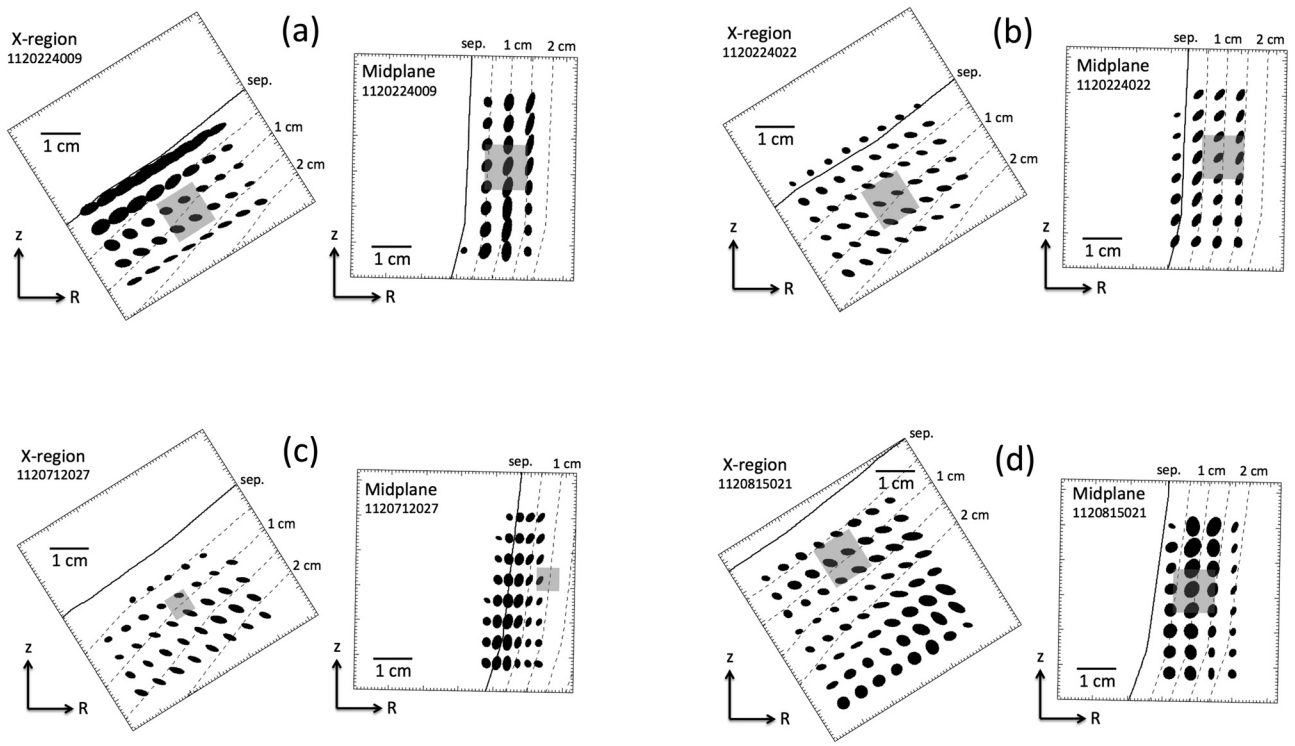

FIG. 5. Typical shapes of the cross-correlations in the X-region (left) and midplane (right) for four typical shots. These maps are drawn for the same regions as Figs. 2 and 4 and oriented in the same direction. The shapes and tilt direction of the black ellipses are defined at a spatial cross-correlation coefficient of 0.7, but their size is reduced by a factor of 3 so they do not overlap. The gray areas show the central regions used for database analysis.

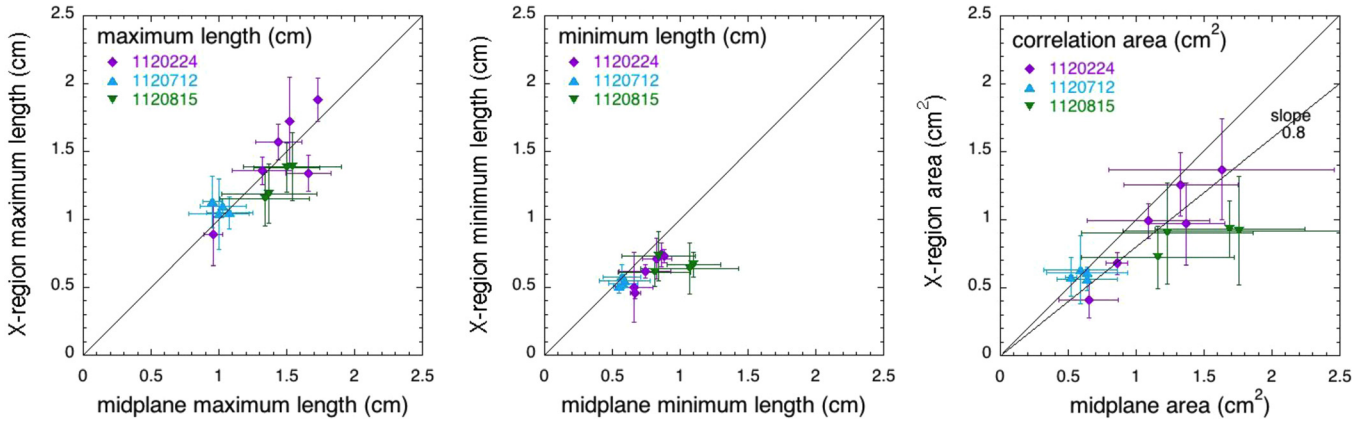

FIG. 6. Comparison between the correlation lengths in the midplane and X-region for all shots of Table I, sorted according to run day. These lengths are based on maps like Figs. 4 and 5, but using only pixels near at the center of the images (gray regions in Fig. 5). At the left are the maximum correlation lengths in the 2D image plane, in the middle are the minimum correlation lengths, and at the right is the area of these correlation structures. If these turbulence followed magnetic flux tubes the areas in the X-region would be ~0.8 that in the midplane due to the 1/R toroidal field, indicated by the line at the right.

correlation lengths in any direction, which were somewhat smaller in the X-region. The product of these lengths, i.e., the area of these correlation structures, was somewhat larger in the midplane region, as shown at the right. The turbulence correlation area in the X-region is roughly 0.8 times that in the midplane view, as indicated by the "slope 0.8" line.

Figure 7 shows a parameterization of the shapes of the 2D turbulence structures for pixels within the same central regions used for Fig. 6 (shown in gray in Fig. 5). For this plot the structure analysis is done for 9 separate points within each of these central regions, and the results are shown separately for each run day. The tilt angles plotted on the vertical axis is the angle at which the cross-correlation function had its maximum length, as measured counter-clockwise from the horizontal major radius direction. The ellipticity plotted on the horizontal axis is the ratio of this largest length to the length perpendicular to this direction (which is nearly the same as the minimum length). The solid symbols in Fig. 7 were based on cross-correlation analysis as used for Fig. 6, while the open symbols were based on a separate blob structure analysis for each shot (see Sec. III E). The tilt angle of the local magnetic flux surfaces with respect to the horizontal (major radius) direction is also shown as the horizontal bars in each case.

Despite the considerable (real) scatter, Fig. 7 shows a consistent difference between the tilt angles of these structures in the midplane and X-regions. The major axis of the cross-correlation ellipse is fairly well aligned with the local flux surfaces in the midplane view, with an average tilt of the major axis of the cross-correlation ellipses of $16° \pm 7°$ (clockwise) from the local flux surfaces, averaged over all shots. However, the average tilt of the cross-correlation functions is $42° \pm 7°$ (clockwise) from the local flux surface for the X-region view, as illustrated in Fig. 4. Thus the turbulence structures are rotated ~25° more (clockwise) with respect to the local flux surfaces in the X-region view than in the midplane view, at least near the $\rho = 1$ analyzed here. Note that a perfectly circular flux tube at the outer midplane develops a slight clockwise tilt even at a small distance below the midplane (see Fig. 1), similar to the tilt in the midplane

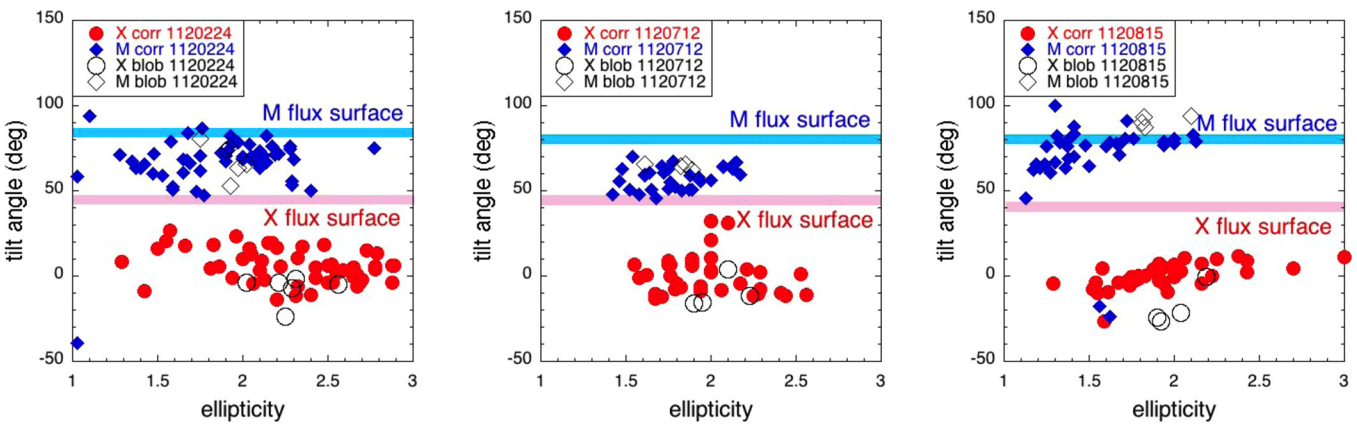

FIG. 7. Parameterization of the shapes of the 2D turbulence structures for the central regions used for Fig. 6, but now plotting separately each pixel for each run day. The tilt angle plotted on the vertical axis of Fig. 7 is the angle at which the cross-correlation function had its largest length, as measured counter-clockwise from the horizontal major radius direction. The ellipticity plotted on the horizontal axis is the ratio of this largest length to the length perpendicular to this direction (nearly the same as the minimum length). The solid symbols in Fig. 7 were based on cross-correlation analysis, as for Fig. 6, while the open symbols were based on a blob structure analysis for each shot (see Sec. III E). The local tilt of the magnetic flux surfaces is shown by the horizontal bars in each case.

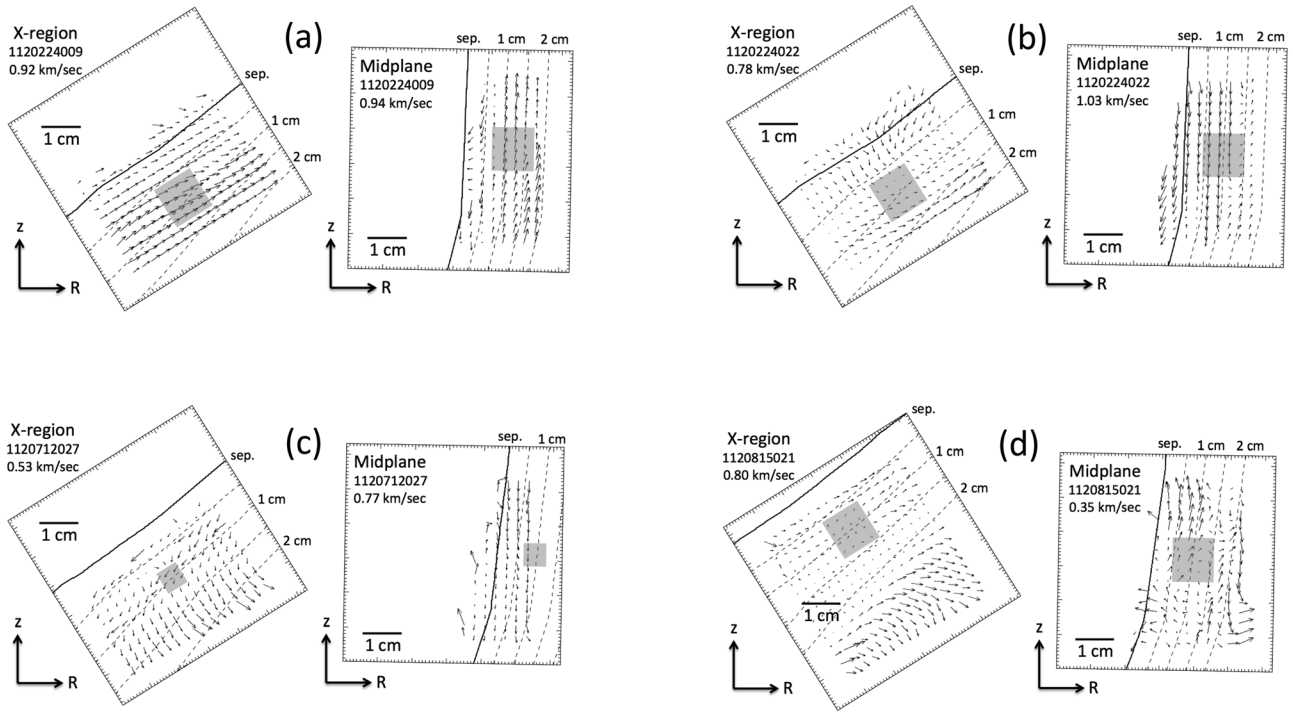

FIG. 8. Typical 2D maps of the time-averaged velocity vectors for the X-region (left) and the midplane (right) for four shots. The orientation is the same as for Fig. 5, and the images are overlaid with the separatrix (solid line) and flux surfaces at 0.5 cm radial intervals (dashed lines). Velocity vectors are shown for every third pixel for the regions with good signal levels. These vectors are drawn with a maximum velocity for each shot specified in the upper left corner of each image, and scaled according to this velocity for each image separately. These velocity maps show rather complex flow patterns which can vary significantly within and between these two GPI views. The gray regions near $\rho = 1$ cm are used for database analysis.

GPI view in Fig. 7. The average ellipticity for the central image region of Fig. 7 is 1.7 ± 0.3 for the midplane view and 2.1 ± 0.3 for the X-region view, which is marginally larger for the X-region. A comparison of these turbulence structures with the magnetic flux tube model is discussed in Sec. V A.

C. Turbulence motion

The time-averaged 2D turbulence velocity fields in both the midplane and the X-region images were evaluated using the time-delayed cross-correlation method described in Sec. III C. This analysis was done for every shot in Table I for time-averaging periods of 3-5 ms (1200–2000 frames).

Figure 8 shows 2D maps of the velocity vectors for the X-region (left) and the midplane (right) for the same four shots as in Fig. 5. The orientation is the same as for Fig. 5, overlaid with the separatrix (solid line) and SOL flux surfaces at 0.5 cm radial intervals (dashed lines). Velocity vectors are shown for every third pixel for the regions with good signal levels, as in Fig. 2. These vectors are drawn with a maximum velocity for each shot specified in the corner of each image, and scaled according to this velocity for each image

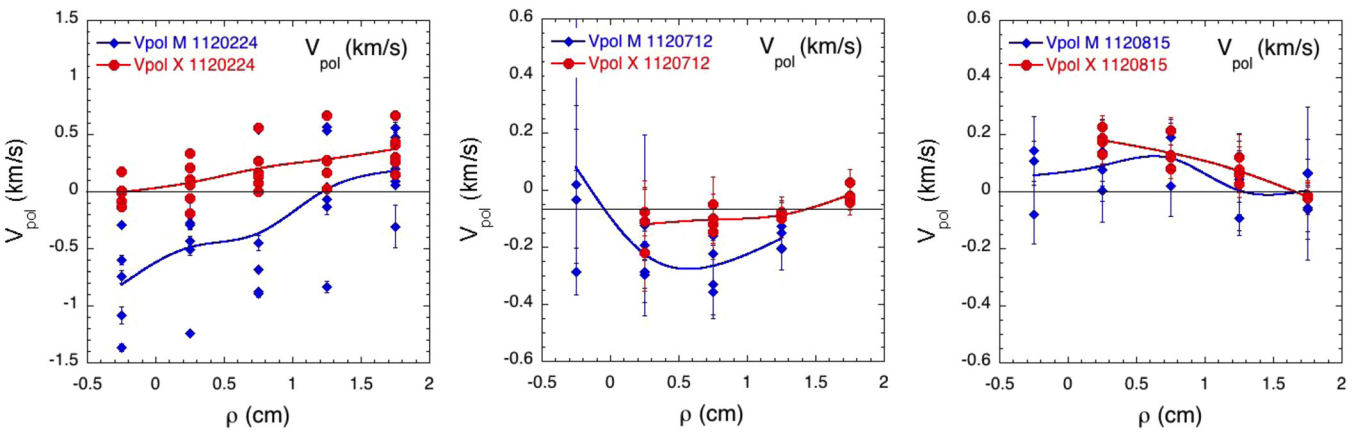

FIG. 9. Comparisons between radial profiles of the poloidal velocities V_{pol} between the midplane and the X-regions, found by averaging over radial zones of width 0.5 cm in maps like those of Fig. 8. Each point in Fig. 9 represents one shot and has an error bars showing the standard deviations of V_{pol} over the ~20-30 pixels in that radial zone for that shot (note the different vertical scales). The V_{pol} profiles of 1120224 are significantly different between midplane and X-region views (i.e., largely outside the mutual error bars), with a dominantly positive (electron diamagnetic direction) turbulence velocity in the X-region view and a dominantly electron diamagnetic velocity in the midplane view.

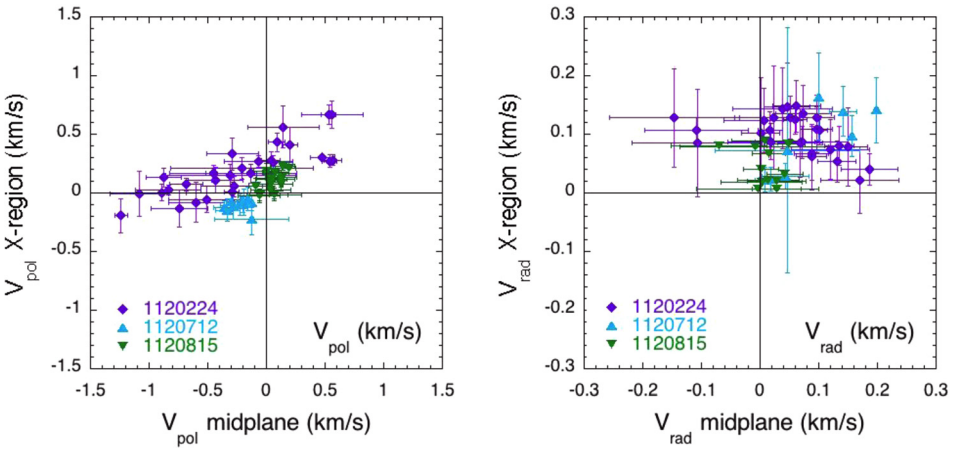

FIG. 10. The same radial profile data as in Fig. 9, but now ploting the midplane velocity vs. the X-region velocity for all shots and radii. At the left are the poloidal velocities and at the right are the radial velocities, all sorted in color by run day as for Fig. 6. The radial velocities are almost all positive (outward radially), and significantly smaller than the poloidal velocities (note the change in velocity scales). The few negative radial velocities are for points near the separatrix.

separately. The velocities at the edges are not shown because the full correlation search over ± 8 pixels could not be completed.

These time-averaged velocity maps show complex flow patterns which can vary significantly between these two GPI views (see movies in "Integral Multimedia"). In some cases like 1120224009, the direction of the turbulence velocity is largely constant within the SOL of each view, but the direction with respect to the local flux surfaces is different between the two views, i.e., with relatively larger radial component in the X-region. The midplane velocity vectors can be either upward as in 1120224009 (electron diamagnetic direction), or downward as in 1120224022. The X-region velocities can vary significantly in both direction and magnitude; for example, there appears to be a circulation in the X-region near $\rho = 1$ cm in 1120224022, and outside $\rho = 2$ cm in 1120815021, but these two circulations are in opposite directions. There is occasionally a localized change in direction within a distance of a few centimeters, such as in the X-region near $\rho = 1$ cm for 1120712026, and in the midplane outside $\rho = 2$ cm in 1120815021. However, there are also similarities in the velocity fields within a given run day; for example, shots 1120224015, 112022423 and 1120224024 look qualitatively similar to 1120224022, and shot 1120224027 looks similar to 1120224009, and all four shots within runs 1120712 and 1120815 look qualitatively similar to each other. It is possible that some of the consistent run-to-run variation is due to the presence or absence of ion cyclotron resonance heating (ICRF) heating, since it has been shown[14] that large potentials can be induced by the ICRF on flux tubes that pass close to or intersect active antennas (see Sec. V C).

Figure 9 shows comparisons between the radial profiles of poloidal velocities V_{pol} in the midplane and X-regions, found by averaging over radial zones of width 0.5 cm in maps like those of Fig. 8. Each point in Fig. 9 represents one shot and has an error bar showing the standard deviations of V_{pol} over the ~20–30 pixels in that radial zone for that shot (note the different vertical scales). The lines shown are cubic spline fits of the midplane and X-region data separately. The V_{pol} profiles of the shots for run #1 are significantly different between midplane and X-region views (i.e., largely outside the mutual error bars), with a dominantly positive (electron direction) turbulence velocity in the X-region view and a dominantly negative turbulence velocity in the midplane view. The average poloidal velocities in the midplane and X-region velocities in runs #2 and #3 are considerably smaller than for #1, but the variations within each radial zone for each shot (indicated by error bars) are comparable to the time-averaged velocities. The small-scale details of the velocities are not the same in the two fields of view, as illustrated in Fig. 8.

Figure 10 shows the same data as in Fig. 9 but now with the midplane velocity plotted vs. the X-region velocity at each radius for each shot. At the left are the poloidal velocities and at the right are the radial velocities, sorted in color by run day as for Fig. 6. There is a partial linear correlation (59%) between V_{pol} in the midplane and V_{pol} in the

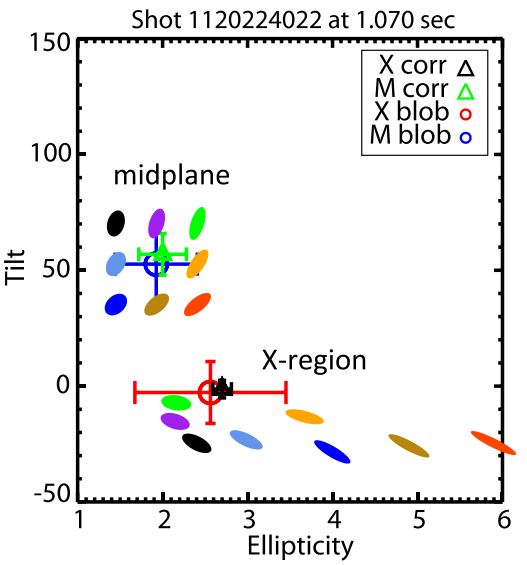

FIG. 11. Comparison of the measured turbulence structure in both GPI views with the magnetic flux tube model. The experimental data are the same as in Fig. 5 but here for a single shot for the central regions near $\rho = 1$ cm, analyzed either using cross-correlations (triangles) or blob analysis (circles). The colored ellipses show the mapping of flux tubes for this shot for an assumed radial location $\rho = 1$, starting from the midplane (where they are fit to the data) and ending where they reach the X-region region (bottom). The shape and tilt of these ellipses reflect their location on this plot.

X-region, although the velocity is often negative in the midplane while positive in the X-region. The radial velocities are almost all positive (radially outward), but significantly smaller than the poloidal velocities (note the change in velocity scales). There does not seem to be any linear correlation between radial velocities in the midplane and X-region, and the few negative radial velocities are only for points near the separatrix. Note that even though the time-averaged velocities in Figs. 9 and 10 are sometimes nearly zero, the small-scale turbulence structures are still in motion, but without any consistent direction, as can be seen in the movies in the "Integral Multimedia," and at Ref. 44.

D. Additional experimental results

This section summarizes some additional experimental results which were obtained from the analysis of these data. For a more detailed description of these results, the reader is referred to the longer report version of this paper.[50]

Analysis of turbulence velocity *fluctuations* was also done for this data set using the technique described previously.[13] Most shots in this database did not have significant correlated fluctuations in the poloidal turbulence velocity between the midplane and X-region views. However, a few of the shots on one run day (run #1) did have a low frequency coherent oscillation in the SOL, in which there was a partial correlation between the midplane and X-regions. The longer term time behavior of turbulence in both the midplane and the X-regions was also analyzed using 10 adjacent time intervals of 5 ms each for several shots. Normally, the structure and motion of the turbulence were nearly constant over 50 ms. The only clear exceptions were during ELMs or L-H transitions when the turbulence changed significant during these transient events.

Some additional analysis was done of the dependence of the turbulence tilt angle and ellipticity on the local turbulence velocity near the center of the fields of view. For both the midplane and the X-region views there was only a slight increase in the tilt angle with increasing (positive) poloidal velocity, and no clear dependence of the ellipticity with poloidal velocity, consistent with the idea that the turbulence structure should have little or no dependence on the local turbulence velocity itself. There was no clear trend in the turbulence tilt angles or ellipticity as a function of the local radial velocity gradient, although there was considerable uncertainty in this evaluation of these gradients (see Fig. 9). The largest radial velocity gradients were $\sim$1 km/s/cm for three shots in the midplane view for run #1, while for most other cases the velocity gradient was $\leq$0.3 km/s/cm. An attempt was also made to evaluate the curl of the local velocity fields, but no significant trends were seen in the turbulence structure with this parameter.

V. DISCUSSION

This section discusses the results of Sec. IV with respect to theory and to previous experiments. Section V A is a discussion of the turbulence structure, and Sec. V B is a discussion of the turbulence velocity, and other physics issues are discussed in Sec. V C. The relationship of these results to previous experiments is discussed in Sec. V D, and Sec. V E presents a summary and conclusions.

A. Turbulence structure *vs.* the flux tube model

The main results on turbulence structure in Sec. IV B and Figs. 4–7 were that the tilt of the turbulent structures in the (R,z) plane was significantly different in the midplane and X-region, and that the elongation and area of the turbulent structures were slightly different in these two regions. This section compares these results with a simple magnetic flux tube model, which assumes that the turbulence structure follows magnetic flux tubes toroidally and poloidal around the SOL, as illustrated in Fig. 1.

Figure 11 compares the measured turbulence structure with the magnetic flux tube model for a specific shot (1120224022). The experimental data points are the same as shown in Fig. 7 for the central region near $\rho = 1$ cm (i.e., the gray areas in Fig. 5), but now labeled with triangles for the cross-correlation analysis and open circles for the blob analysis, with error bars showing the standard deviations in this region. The solid colored ellipses show the tilt (measured with respect to the major radius direction) and the ellipticity of magnetic flux tubes in this plane. These flux tubes are started at the midplane with a range of tilt and ellipticity overlapping the measured values, and are ended when they reach the (R,z) coordinates of the X-region view (bottom). If the turbulence followed magnetic field lines, the measured X-region tilt and ellipticity should agree with the calculated flux tube shapes for the X-region.

The result of Fig. 11 is that there is partial (but far from perfect) agreement between the observed X-region turbulence structure and the simple magnetic flux tube model. The measured tilts in the X-region are nearly in the major radius direction ($\sim$0°), whereas the calculated tilts are $\sim$20° $\pm$ 10° more clockwise, as shown in Fig. 1. The measured ellipticity in the X-region is $\sim$2, whereas the calculated ellipticity is $\sim 4 \pm 2$. There is a similar level of (dis)agreement of the observed X-region structure with the flux tube model for two other shots from other run days in this experiment. These differences cannot be accounted for by variations in the radial location of the assumed flux surfaces in the model over $\rho = 1.0 \pm 0.5$ cm, which are typically $\pm$5° in tilt and $\pm$0.4 in ellipticity. Some distortions in the observed turbulence structure may also be caused by the slight misalignments of the viewing angle with respect to the local B field, as discussed in Sec. III G, but these are not large enough to cause the disagreement between the data and the model for the X-region in Fig. 11.

Another point of comparison between the turbulence structure and the flux tube model is the relative spatial scale of the turbulence in the two regions. The measured area of the structures as shown in Fig. 6 was roughly 0.8 times smaller in the X-region than in the midplane view, which is similar to the expected area ratio if the turbulence followed magnetic flux tubes ($R_X/R_{mid} \sim 0.78$), although there is a considerable scatter in the data. The maximum length of the flux tube cross-sections in Fig. 11 increases by a factor of $\sim$2 from the midplane to the X-region, but the measured

turbulence structures do not significantly increase in maximum length, which disagrees with this model. Thus, the overall result is only a partial agreement with the simple magnetic flux tube model.

There are at several possible reasons why the magnetic flux tube model only partially explains the observed variations of the turbulence structure between these two viewing regions. First, flow shear could distort the SOL filaments between the two views (see Sec. V B). Second, the flux tube model assumes that the turbulence has the same structure at different toroidal angles, which ignores the non-axisymmetric effects of the RF antennas (see end of Sec. V B). Third, the SOL filaments could become partially disconnected along B field lines due to collisions or magnetic field shear (see Sec. V C). Finally, the measurements may be responding to a basic difference between electron density and temperature fluctuations (see Sec. V D). A clear experimental discrimination among these alternatives cannot yet be made.

B. Turbulence motion *vs.* plasma flows

The main results on turbulence motion in Sec. IV C and Figs. 8–10 can be summarized as follows: the time-averaged poloidal velocity of the turbulence was often different in the X-region and midplane view (sometimes even in a different direction), and the time-averaged radial turbulence velocity was generally smaller than the poloidal velocity, but similar in magnitude (although uncorrelated) in the two viewing regions. There were also complex velocity variations within both regions for a given shot, and large differences from run-to-run.

For these experiments, the ∇B drift, curvature drift, and ion diamagnetic drift directions are all downward in the GPI viewing regions. The poloidal $E \times B$ velocity in Ohmically heated plasmas should be dominated by the sheath potential $\Phi(r) \sim 3T_e(r)/e$, where T_e is the electron temperature in the SOL. The resulting radial electric fields should be $\sim 3T_e/L_{Te} \sim 100$ V/cm, and corresponding $E \times B$ poloidal velocities are $\sim$2 km/s downward, based on the midplane electron temperatures (see Sec. II and Table II). This is significantly larger than the typical velocities for the Ohmic run #2 in Fig. 9, which showed downward (i.e., negative) velocities of up to $\sim$0.3 km/s. This source of $E \times B$ motion cannot explain the positive (upward) poloidal velocities shown for runs #1 and #3 of Fig. 9. The diamagnetic velocity in the SOL should be roughly $V_d = (kT/eB)/L_n \sim 0.5$ km/s for the parameters of Table II, either in the positive (upward) direction for electrons or in the negative (downward) direction for ions. However, it is not clear whether the turbulence should propagate in the electron or ion diamagnetic direction in the rest frame of the plasma, since this apparently depends on the nature of the turbulence. Therefore, we cannot clearly identify the poloidal turbulence flow in this experiment with either the local $E \times B$ or diamagnetic flows.

The radial turbulence velocities of $\sim$0.1 km/s shown in Fig. 10 are similar to those inferred from both particle balance and turbulent transport in Ref. 15, but the results of Fig. 10 show no systematic difference between the radial turbulence velocities in the midplane and X-region, suggesting that the radial transport is not much different at these two poloidal angles.

Consider next how the perpendicular flow may be expected to vary poloidally in a quiescent SOL. We may expect the potential Φ, the pressure p, and the density n to be nearly constant on field lines between the two observation regions.[51] The magnitude of the perpendicular flow velocity is then the sum of the $E \times B$ and ion diamagnetic drift velocities $|B^{-2}\mathbf{B} \times \nabla\Phi + (neB^2)^{-1}\mathbf{B} \times \nabla p| = \omega|\nabla\psi|/B$ where $2\pi\psi$ is the magnetic flux and $\omega = d\Phi/d\psi + (ne)^{-1}dp/d\psi$ is nearly constant. Notice $|\nabla\psi| = 1/$(distance between ψ contours), so $|\nabla\psi|$ is slightly larger at the midplane, while B is slightly smaller at the midplane. Thus, in the context of this model, the flows at the midplane location should be slightly larger than at the X-point location, and both would be downward. This is apparently not consistent with the turbulence velocity profiles of Fig. 9.

The disagreements between the observed turbulence structure and the magnetic flux tube model of Fig. 11 could in part be due to the $E \times B$ flow shear, which should affect turbulence when $S = (dV_{pol}/dr)(L_{rad}/L_{pol})\tau \geq 1$, where dV_{pol}/dr is the radial gradient of the poloidal turbulence velocity, L_{rad} and L_{pol} are the turbulence scale lengths, and τ is the turbulence autocorrelation time. Some direct evidence for this turbulence tilting was recently seen in NSTX[23] and Tore Supra,[16] and in linear devices such as LAPD,[52] in which flow shear can be imposed by external biasing. There are clearly gradients in the time-averaged poloidal turbulence velocity, as shown in Fig. 9 and discussed briefly in Sec. IV D. If these gradients are assumed cause turbulence shearing, a typical normalized shear is $S = (0.3\ \text{km/s/cm})\ (1\ \text{cm}/1\ \text{cm})\ (30\ \mu\text{s}) \sim 1$, which is marginal for affecting the turbulent structure (the time-dependent velocity shearing could be larger than this, but was not evaluated in detail for these experiments). If this $E \times B$-induced shear flow was not constant along B, e.g., due to the spatial distortion of the flux tubes along B or to the finite ion parallel propagation time, then the $E \times B$ shearing effects could be different in these two poloidal regions.

Another unresolved issue in these experiments is the effect of the ICRF-induced potentials on the radial electric fields, which has been shown to be present in the C-Mod SOL during ICRF heating.[14] The $E_r \times B$ flows driven by this effect are quite large on flux tubes that magnetically map to or just in front of active antennas. These potentials are seen to penetrate up to $\sim$1 cm into the SOL from the radius of the antenna faces and, because the entire flux tube is affected, are not localized to the toroidal extent of the antennas. The spatial-scale in the radial direction can be sub-cm, typically$\sim$0.5 cm. This E_r can be negative (typical) or positive depending on whether the affected field-line is radially inward or outward of the antenna face, and thus can induce flows in either direction. Since at least two of C-Mod's antennas were active during the times of interest during the runs #1 and #3, this effect will complicate the interpretation of velocities not on the same flux tube for these runs. Run #2 had no ICRF heating; however, these shots had an extremely small outer gap ($\sim$0.1 cm) between the last closed flux

surface (LCFS) and the innermost outboard limiter (see Table I). As a result, those SOL field-lines with $\rho > 0.1$ cm may be intercepted by toroidally discrete structures resulting in significantly different connection lengths. Comparisons of the connection lengths within each view at the same ρ show differences of factors of 1.3 to 8 for ρ values >0.5 cm for these shots. Thus, there is no toroidal symmetry for those ρ regions of the views, and SOL turbulence may not be the same given those different field-line boundary conditions. Additional toroidal non-axisymmetries could be due to neutral and/or impurity sources, although the effect of these on the SOL turbulence is not known.

A final issue in the interpretation of the turbulence velocities concerns the slight extent to which the GPI cameras are not pointed perfectly parallel to the total B field. Flow along B may then appear in the cameras as either toward or away from the X-point depending on whether the pitch of the camera view is greater or less than the pitch of the field. Average parallel flow arises in the edge due to several factors, including Pfirsch-Schlüter effects,[15] collisional (neoclassical) flow,[53] and sources and sinks.[54] For these two GPI views the misalignment angles were $\leq 1°$-$2°$ (see Sec. III G), so if the parallel velocities in the SOL were $\leq$20 km/s (i.e., about half the ion sound speed), then these apparent velocities could be $\leq$0.5 km/s. Therefore, this effect might also contribute to the poloidal (or radial) turbulence velocities measured by the GPI cameras (and in the GPI photodiodes, which were misaligned by $\sim 11°$). Unfortunately, this effect cannot be further evaluated without more information about the magnitude of the local parallel flow speed in these two views for these shots.

C. Turbulence structure and motion *vs.* blob models

In the low beta ideal MHD limit of the theory of SOL blob-filaments,[19] if the perpendicular viscosity is sufficiently large the whole blob-filament moves as a rigid flux-tube structure. In this limit, one would expect that midplane and X-region velocities should be well correlated. There is some evidence for poloidal velocity correlation in Fig. 10, but evidently the large viscosity limit is not strictly applicable to the present dataset. In the highly collisional limit where local perpendicular 2D dynamics applies, we expect a localized blob to move primarily in the major radial ($-\nabla$B) direction, which according to Fig. 1 should give comparable radial and poloidal velocities in the X-region. This does not seem to agree with Fig. 10 for run #1, but is not far off for the other two run days.

The local curvature-driven blob velocity can be estimated from Eq. (11) of Ref. 55 as: $V_{blob} = c_s\ f_b\ (\delta_b/R)^{1/2}$, where c_s is the ion sound speed, $f_b = \delta p/p_0 < 1$ is an amplitude factor, and δ_b is the blob radius. Here, finite background plasma pressure p_0 (or equivalently finite blob amplitude δp relative to p_0) affects the blob speed because it changes the effective gradient scale length $(\nabla p/p_0)^{-1}$ that drives the convection. This is roughly accounted for by the factor $f_b \sim 0.3$. For this experiment $V_{blob} \sim (2 \times 10^6$ cm/s) (0.3) (1 cm/100 cm)$^{1/2} \sim 0.5$ km/s, which is higher than the measured radial turbulence velocities of $\sim$0.1 km/s in Fig. 10. This is not surprising as the theoretical V_{blob} scaling quoted here for the sheath-disconnected or inertial regime is effectively an upper bound. Any effects which drain or neutralize the local curvature-induced polarization charges (such as parallel currents to the sheath or friction) will slow the blob down. Regime estimates given below suggest only marginal sheath disconnection and thus may point to some slowing by parallel current. The effect of neutral friction in reducing the blob velocity[56,57] may also not be negligible. When ion-neutral friction is large and dominates inertia $V_{blob} \sim c_s^2 f_b/(\nu_{i0} R)$ where ν_{i0} is the ion-neutral collision frequency. Unfortunately, there is no direct measurement of the neutral density ($\propto \nu_{i0}$) in these experiments, thus a quantitative comparison with this limit is not possible.

The major radial stretching of structures observed in the X-region (i.e., a tilt angle $\sim 0°$) might be driven by the local curvature in the X-region, which is predominantly in the R direction due to the dominant toroidal curvature. The flux tube mapping model and Ryutov's model of blobs[19] are for ideal MHD. However, if we consider the opposite extreme limit of highly resistive MHD, then there is negligible parallel current, so each perpendicular slice of blob propagates independently of the others, all moving in the local $-\nabla$B direction. In this 2D limit we would expect the X-region structures to move primarily outward in R, and not to follow the magnetic flux tube mapping model.

The highly resistive limit is defined by a dimensionless collisionality $\Lambda > 1$,[23] where the collisionality parameter $\Lambda = L_{||}\nu_{ei}/(\rho_s\ \Omega_e)$ may also be written as $\Lambda = (m_e/m_i)^{1/2}\ \nu_{e*}$, where the dimensionless collisionality $\nu_{e*} = L_{||}/\lambda_{ei}$ ($L_{||}$ is the shortest distance to the divertor plate along a field line, and λ_{ei} is the electron mean free path for collisions with ions). There is quite a range in lambda, given the stated uncertainties in n_e and T_e in Table II, even taking $L_{||}$ as fixed. For L-mode the range is $\Lambda \sim 0.15$ to 0.85 and for H-mode the range is $\Lambda \sim 1.1$ to 2.2. Blob filaments are expected[6] to become collisionally disconnected from the divertor plate sheaths when Λ exceeds a critical value which is always less than order unity. The critical value is reduced below one by magnetic shear effects that can be estimated from the ellipticity, i.e., the ratio of major to minor radii of the ellipse traced out by field line mapping. Thus, in both the H-mode and L-mode cases the midplane region is at least marginally collisionally disconnected from the sheaths, since ellipticity > 2 is calculated for flux tubes near the X-region GPI (see Fig. 11). Note that both the minimum width of the measured turbulence and also the calculated flux tubes in the X-region (Figs. 6 and 11) are both much larger than the ion gyroradius of $\sim 10^{-2}$ cm (Table II), so magnetic flux tube disconnection effects from finite ρ_i [e.g., 6] are probably negligible here.

A separate condition can be given for when the dynamics of two locations on a field line separated by $L_{||}$ become de-correlated due to collisions, i.e., when perpendicular polarization currents become more important than parallel currents. This condition is given by $\Lambda > (\delta_b/\delta_*)^{5/2}$ where δ_b is the blob radius and $\delta_* = \rho_s (L_{||}^2/\rho_s R)^{1/5}$. For the present dataset $\delta_* \sim 0.15$–0.2 cm and $\delta_b \sim 0.5$–1.5 cm (e.g., from Fig. 6), so $(\delta_b/\delta_*)^{5/2} \sim$ 8–300 and collisional decorrelation of midplane and X-region locations (where they on the same

field line) should not occur. In this limit, the grad-B outward force is averaged along the filament and applied to the filament dynamics as a whole, as opposed to acting locally on a cross-section of the filament. This is consistent with the observation that some correlation along the field lines has been observed in other C-Mod experiments.[4]

D. Relationship between density and temperature fluctuations

An interesting complication in interpreting the X-region data comes about from a combined effect of the 3D dynamics and the fact that the He line emission measured by GPI depends on both T_e and n_e. We expect T_e to be communicated rapidly along the field line at v_e (or somewhat slower in conduction-limited regimes), but n_e to be communicated at the much slower speed $\sim c_s$. For example, if $L_{\|} \sim 3$ m between these views and $T_e = 20$ eV, the parallel communication time for ions and electrons would $\sim 100\,\mu$s and $\sim 2\,\mu$s, respectively (at c_s and v_e), while the turbulence autocorrelation time is ~ 20–$50\,\mu$s (Fig. 3). Thus if we imagine the plasma is first ejected from the closed flux surfaces near the outer midplane,[21,23] then the T_e and the electrostatic potential of this perturbation will arrive at the X-region well within a turbulence correlation time, but the density arrives at the X-region only after a parallel ion transit time. Therefore, the density fluctuations in the X-region may involve a convolution of parallel propagation and simultaneous radial motion across the local density gradient in the X-region.

The expected contribution to the density fluctuations from the local density gradient in the X-region is $\nabla n = \tilde{n} \nabla n$.[58] However, the local ∇n in the X-region is not measured in this experiment and the turbulent fluctuation level is large, so it is not possible to measure the relative contributions of the perpendicular and parallel sources to the local density fluctuations in the X-region. The calculated dependence of the HeI light emission on density and T_e fluctuations near $\rho = 0.5$ cm (Table II) is $\sim n^{0.13}\, T_e^{0.4}$, which implies a relatively weak density dependence in this region, which will tend to reduce the effects of density fluctuations on the GPI signal fluctuations. The result is that there is presently an uncertain effect of the mixture of density and electron temperature fluctuations on the structure of turbulence in the X-region.

We note that previous measurements in tokamaks showing high correlations along B did not completely separate the effects of electron density and temperature fluctuations. For example, the correlation measurements in JET[3] were made using ion saturation currents, which are sensitive to electron temperature fluctuations as well as density fluctuations. The GPI/LiI correlations along B made optically in NSTX[5] may also have been measuring dominately electron temperature fluctuations. The parallel correlation measurements done in C-Mod[4] and NSTX[45] used both GPI and ion saturation currents, so their correlations could also have partially been measuring electron temperature fluctuations.

E. Summary and conclusions

This paper described 2D imaging of plasma turbulence in the scrape-off layer of the Alcator C-Mod tokamak at two different poloidal locations, one near the outer midplane and the other near the divertor X-point region. These images were made simultaneously with radial vs. poloidal resolution using two gas puff imaging diagnostics.

The main experimental results were as follows:

(1) The basic turbulence characteristics were similar between the midplane and X-point region, as shown in Fig. 3 and described in Sec. IV A.
(2) The tilt angle and area of the turbulent structures were significantly different in the midplane and X-regions, as shown in Figs. 4–7 and described in Sec. IV B.
(3) The poloidal turbulence velocity was sometimes significantly different between the midplane and the X-regions, as shown in Figs. 8–10 and described in Sec. IV C.
(4) Some other new results were that the turbulence structure in the midplane view was systematically tilted with respect to the local flux surfaces (Fig. 7), the turbulence velocity sometimes had variable and complex small-scale features within each view (Fig. 8), and the turbulence could move in different poloidal directions in the two views (Figs. 9 and 10).

Several possible interpretations of these results were discussed in Sec. V. The simple magnetic flux tube model of turbulence structure only partially explained the variation of tilt angle and ellipticity between these two poloidal regions,

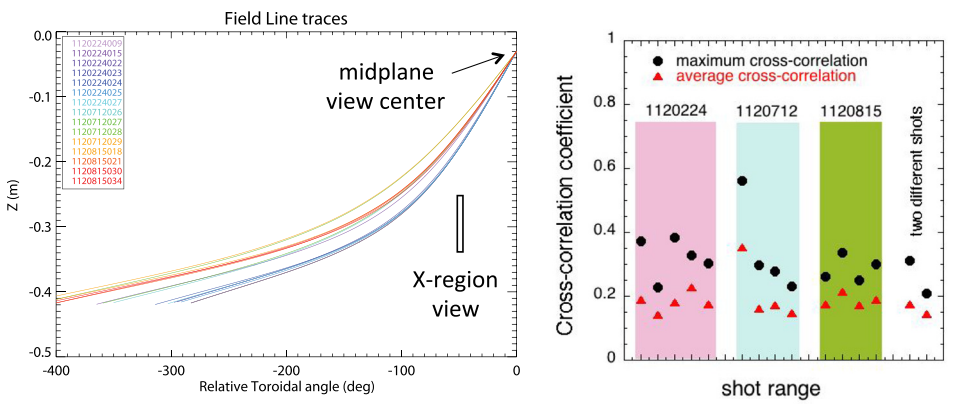

FIG. 12. At the left is a map showing the toroidal vs. vertical trajectories of magnetic field lines at starting $\rho = 1$ cm in the midplane viewing region for all shots in this experiment, with the location of the X-region GPI view indicated by the black box. The plot on the right is the measured average and maximum cross-correlation coefficient of the turbulence between the two views for each shot, and between two different shots (right). Except for one shot (1120712026) there is little or no significant cross-correlation, as expected from the mapping.

as shown in Fig. 11 and discussed in Sec. V A. The difference observed in the poloidal turbulence velocity between the two regions could be due to E × B shear flow, to localized ICRH-induced electric fields, or to the possible effects of parallel flow on the measurements, as discussed in Sec. V B. An evaluation of blob models showed that the SOL turbulence is marginally collisionally disconnected between these regions, as discussed in Sec. V C. Finally, the possible differences between density and electron temperature fluctuations, and how this could affect the interpretation of these results, were discussed in Sec. V D.

There are many directions for future research in this area. The various uncertainties and limitations of the GPI diagnostic and data analysis described in Sec. III G could be reduced with hardware and software improvements. Additional GPI measurements could be made at other poloidal and toroidal angles to clarify the full 3D edge turbulence structure, and direct comparisons with other edge turbulence and/or flow diagnostics would be very valuable. These experiments should be repeated without the complicating feature of ICRF-heating and the large SOL radial electric field typically observed with the ICRF in C-Mod, and with larger outer "gaps" so that the toroidal symmetry is better preserved in the SOL. The turbulence velocities derived from cross-correlation analysis should be compared with turbulence phase velocities derived from frequency vs. wavenumber analysis. More detailed modeling of the GPI diagnostic resolution and sensitivity could be done using a neutral code such as DEGAS 2, given additional edge temperature and density profile data and 3D imaging of the GPI gas cloud. Finally, 3D turbulence simulations need to be done to understand these results and predict the effects of this turbulence on SOL transport in future tokamaks.

ACKNOWLEDGMENTS

We thank D. A. D'Ippolito, E. Feibush, S. Krasheninnikov, R. J. Maqueda, T. Munsat, D. A. Russell, B. D. Scott, M. V. Umansky, and G. S. Xu for their contributions and/or comments on this paper. S. J. Zweben would like to thank the Alcator C-Mod group for their long-term support for this research, which was funded in part by US DOE Contracts DE-AC02-09CH11466 and DE-FC02-99ER5412.

APPENDIX: MAGNETIC FIELD LINE MAPPING

At the left of Fig. 12 is a toroidal vs. z-coordinate map of magnetic field lines starting from the vertical center of the midplane view at $\rho = 1$ cm, i.e., at $z = -3$ cm and toroidal angle = 0. None of these B field lines intersect the X-region view, the projection of which onto $R = R_{view\ center}$ plane is indicated by the black box. This is not surprising since these GPI views were not designed to be on the same field line. Other field lines started from $\rho = 2$ cm and at $\rho = 0.2$ cm (from $z = -6$ cm and $\phi = 0$, the lowest point in the midplane view) also do not intersect the X-region view, with the closest approach being ~11 cm. This suggests that there should be little or no cross-correlation between turbulence in these two views, based on the flux tube mapping model.

At the right of this figure is an analysis of the actual cross-correlation of the turbulence between the midplane and the X-region views for all shots in Table I. This was done by correlating every third pixel in the midplane region with all pixels in the X-region using time delays of up to ±2 frames (±4.2 μs), i.e., in the time delay range of turbulence cross-correlations along a B field line.[4] The average cross-correlations are shown by the triangles, and the maximum cross-correlations are shown by the circles. These data are grouped according to run day, and the random level of cross-correlation is evaluated by using the midplane data from one shot and the X-region data from another shot (1120712026 and 027), and vice versa, as shown at the right. The result is that there was no significant cross-correlation between the turbulence in the midplane and X-region views, except for one shot (1120712026). The higher cross-correlation for 1120712026 appears to be due to a macroscopic global fluctuation that is apparent on both GPI signals as well as a D_α emission monitor viewing neither of the GPI regions.

[1]S. J. Zweben, J. A. Boedo, O. Grulke, C. Hidalgo, B. LaBombard, R. J. Maqueda, P. Scarin, and J. L. Terry, Plasma Phys. Controlled Fusion **49**, S1 (2007).
[2]J. A. Boedo, J. Nucl. Mater. **390–391**, 29 (2009).
[3]H. Thomsen, M. Endler, J. Bleul, A. V. Chankin, S. K. Erents, G. F. Matthews, and Contributors to the EFDA-JET Work Programme, Phys. Plasmas **9**, 1233 (2002).
[4]O. Grulke, J. L. Terry, B. LaBombard, and S. J. Zweben, Phys. Plasmas **13**, 012306 (2006).
[5]R. Maqueda, D. P. Stotler, and NSTX Team, Nucl. Fusion **50**, 075002 (2010).
[6]D. D'Ippolito, J. R. Myra, S. J. Zweben *et al.*, Phys. Plasmas **18**, 060501 (2011).
[7]J. R. Angus, S. I. Krasheninnikov, and M. Umansky, Phys. Plasmas **19**, 082312 (2012).
[8]J. L. Terry, S. J. Zweben, K. Hallatschek, B. LaBombard, R. J. Maqueda, B. Bai, C. J. Boswell, M. Greenwald, D. Kopon, W. M. Nevins, C. S. Pitcher, B. N. Rogers, D. P. Stotler, and X. Q. Xu, Phys. Plasmas **10**, 1739 (2003).
[9]I. Garcia-Cortes, C. Hidalgo, J. R. Martın-Solis, S. Ali-Arshad, S. Clement, S. J. Davies, J. Lingertat, A. Loarte, G. F. Matthews, and R. D. Monk, Plasma Phys. Controlled Fusion **38**, 2051 (1996).
[10]R. A. Moyer, R. Lehmer, J. A. Boedo, J. G. Watkins, X. Xu, J. R. Myra, R. Cohen, D. A. D'Ippolito, T. W. Petrie, and M. J. Schaffer, J. Nucl. Mater. **266–269**, 1145 (1999).
[11]G. Y. Antar, G. Counsell, J.-W. Ahn, Y. Yang, M. Price, A. Tabasso, and A. Kirk, Phys. Plasmas **12**, 032506 (2005).
[12]J. L. Terry, S. J. Zweben, M. V. Umansky, I. Cziegler, O. Grulke, B. LaBombard, and D. P. Stotler, J. Nucl. Mater. **390–391**, 339 (2009).
[13]S. J. Zweben, J. L. Terry, M. Agostini, R. Hager, J. W. Hughes, J. R. Myra, D. C. Pace, and Alcator C-Mod Group, Plasma Phys. Controlled Fusion **54**, 025008 (2012).
[14]I. Cziegler, J. L. Terry, S. J. Wukitch, M. L. Garrett, C. Lau, and Y. Lin, Plasma Phys. Controlled Fusion **54**, 105019 (2012).
[15]N. Smick, B. LaBombard, and I. H. Hutchinson, Nucl. Fusion **53**, 023001 (2013).
[16]N. Fedorczak, P. Manz, S. C. Thakur, M. Xu, G. R. Tynan, G. S. Xu, and S. C. Liu, Phys. Plasmas **19**, 122302 (2012).
[17]S. C. Liu, L. M. Shao, S. J. Zweben, G. S. Xu, H. Y. Guo, B. Cao, H. Q. Wang, L. Wang, N. Yan, S. B. Xia, W. Zhang, R. Chen, L. Chen, S. Y. Ding, H. Xiong, Y. Zhao, B. N. Wan, X. Z. Gong, and X. Gao, Rev. Sci. Instrum. **83**, 123506 (2012).
[18]D. Farina, R. Pozzoli, and D. Ryutov, Plasma Phys. Controlled Fusion **35**, 1271 (1993).
[19]D. D. Ryutov, Phys. Plasmas **13**, 122307 (2006).
[20]J. R. Angus, M. V. Umansky, and S. I. Krasheninnikov, Phys. Rev. Lett. **108**, 215002 (2012).
[21]E. Havlickova, W. Fundamenski, V. Naulin, A. H. Nielsen, R. Zagorski, J. Seidl, and J. Horacek, Plasma Phys. Controlled Fusion **53**, 065004 (2011).

[22]G. Q. Yu, S. I. Krasheninnikov, and P. N. Guzdar, Phys. Plasmas **13**, 042508 (2006).
[23]J. R. Myra, W. M. Davis, D. A. D'Ippolito, B. LaBombard, D. A. Russell, J. L. Terry, and S. J. Zweben, "Edge sheared flows and the dynamics of blob-filaments," paper presented at the 24th IAEA Fusion Energy Conference, San Diego, USA, October 8– 13, 2012, paper IAEA-CN-197/TH/P4-23.
[24]K. Bodi, S. I. Krasheninnikov, and A. I. Smolyakov, Phys. Plasmas **15**, 102304 (2008).
[25]D. A. Baver, J. R. Myra, and M. V. Umansky, Comput. Phys. Commun. **182**, 1610 (2011).
[26]A. Mosetto, F. D. Halpern, S. Jolliet, and P. Ricci, Phys. Plasmas **19**, 112103 (2012).
[27]B. D. Scott, Plasma Phys. Controlled Fusion **49**, S25 (2007).
[28]F. Militello, P. Tamain, W. Fundamenski, A. Kirk, and V. Naulin, Plasma Phys. Controlled Fusion **55**, 025005 (2013).
[29]D. A. Russell, J. R. Myra, D. A. D'Ippolito, T. L. Munsat, Y. Sechrest, R. J. Maqueda, D. P. Stotler, S. J. Zweben, and NSTX Team, Phys. Plasmas **18**, 022306 (2011).
[30]R. H. Cohen, B. LaBombard, D. D. Ryutov, J. L. Terry, M. V. Umansky, X. Q. Xu, and S. Zweben, Nucl. Fusion **47**, 612 (2007).
[31]S. J. Zweben, B. D. Scott, J. L. Terry, B. LaBombard, J. W. Hughes, and D. P. Stotler, Phys. Plasmas **16**, 082505 (2009).
[32]P. Ricci and B. N. Rogers, Phys. Plasmas **20**, 010702 (2013).
[33]W. M. Nevins, M. A. Makowski, J. A. Boedo, D. L. Rudakov, G. R. McKee, Z. Yan, and R. J. Groeber, Phys. Plasmas **20**, 055906 (2013).
[34]S. J. Zweben, R. J. Maqueda, D. P. Stotler, A. Keesee, J. Boedo, C. E. Bush, S. M. Kaye, B. LeBlanc, J. L. Lowrance, V. J. Mastrocola, R. Maingi, N. Nishino, G. Renda, D. W. Swain, J. B. Wilgen, and NSTX Team, Nucl. Fusion **44**, 134 (2004).
[35]M. Agostini, R. Cavazzana, P. Scarin, and G. Serianni, Rev. Sci. Instrum. **77**, 10E513 (2006).
[36]Y. Nakashima, N. Nishino, Y. Higashizono, H. Kawano, S. Kobayashi, M. Shoji, Y. Kubota, M. Yoshikawa, M. K. Islam, Y. Mishima, D. Mimura, and T. Cho, J. Nucl. Mater. **363–365**, 616 (2007).
[37]N. Nishino, T. Mizuuchi, Z. Feng, S. Kobayashi, K. Nagasaki, H. Okada, Y. Torii, K. Kondo, and F. Sano, J. Nucl. Mater. **363–365**, 628 (2007).
[38]I. Shesterikov, Y. Xu, C. Hidalgo, M. Berte, P. Dumortier, M. Van Schoor, M. Vergote, G. Van Oost, and TEXTOR Team, Nucl. Fusion **52**, 042004 (2012).
[39]D. P. Stotler, B. LaBombard, J. L. Terry, and S. J. Zweben, J. Nucl. Mater. **313–316**, 1066 (2003).
[40]D. P. Stotler, J. Boedo, B. LeBlanc, R. J. Maqueda, and S. J. Zweben, J. Nucl. Mater. **363–365**, 686 (2007).
[41]B. Cao, D. P. Stotler, S. J. Zweben, M. Bell, A. Diallo, and B. LeBlanc, Fusion Sci. Technol. **64**, 29 (2013).
[42]J. L. Terry, B. LaBombard, B. Lipschultz, M. J. Greenwald, J. E. Rice, and S. J. Zweben, Fusion Sci. Technol. **51**, 342 (2007).
[43]J. W. Hughes, P. B. Snyder, J. R. Walk, E. M. Davis, A. Diallo, B. LaBombard, S. G. Baek, R. M. Churchill, M. Greenwald, R. J. Groebner, A. E. Hubbard, B. Lipschultz, E. S. Marmar, T. Osborne, M. L. Reinke, J. E. Rice, C. Theiler, J. Terry, A. E. White, D. G. Whyte, S. Wolfe, and X. Q. Xu, Nucl. Fusion **53**, 043016 (2013).
[44]See http://w3.pppl.gov/~szweben/CMod2012both/CMod2012both.html for videos of this GPI imaging data.
[45]S. J. Zweben, R. J. Maqueda, A. L. Roquemore, C. E. Bush, R. Kaita, R. J. Marsala, Y. Raitses, R. H. Cohen, and D. D. Ryutov, Plasma Phys. Controlled Fusion **51**, 105012 (2009).
[46]M. Agostini, R. Cavazzana, P. Scarin, G. Serianni, Y. Yagi, H. Koguchi, S. Kiyama, H. Sakakita, and Y. Hirano, Plasma Phys. Controlled Fusion **50**, 095004 (2008).
[47]T. Munsat and S. J. Zweben, Rev. Sci. Instrum. **77**, 103501 (2006).
[48]B. Tal, A. Bencze, S. Zoletnik, G. Veres, and G. Por, Phys. Plasmas **18**, 122304 (2011).
[49]S. Zoletnik, L. Bardoczi, A. Kramer-Flecken, Y. Xu, I. Shesterikov, S. Soldatov, G. Anda, D. Dunai, G. Petravich, and TEXTOR Team, Plasma Phys. Controlled Fusion **54**, 065007 (2012).
[50]S. J. Zweben, J. L. Terry, M. Agostini, W. M. Davis, A. Diallo, R. A. Ellis, T. Golfinopoulos, O. Grulke, J. W. Hughes, B. LaBombard, M. Landreman, J. R. Myra, D. C. Pace, and D. P. Stotler, "Comparison of edge turbulence imaging at two different poloidal locations in the scrape-off layer of Alcator C-Mod," Princeton Plasma Physics Laboratory Report PPPL-4864, March 2013.
[51]A. N. Simakov, P. J. Catto, B. LaBombard, and A. H. Glasser, Plasma Phys. Controlled Fusion **50**, 105010 (2008).
[52]T. Carter and J. E. Maggs, Phys. Plasmas **16**, 012304 (2009).
[53]M. Landreman and D. Ernst, Plasma Phys. Controlled Fusion **54**, 115006 (2012).
[54]P. Stangeby, *The Plasma Boundary of Magnetic Fusion Devices, Plasma Physics Series* (IOP, Bristol, 2000), Chaps. 15 and 17.
[55]J. R. Myra, D. A. D'Ippolito, D. P. Stotler, S. J. Zweben, B. P. LeBlanc, J. E. Menard, R. J. Maqueda, and J. Boedo, Phys. Plasmas **13**, 092509 (2006).
[56]N. Katz, J. Egedal, W. Fox, A. Le, and M. Porkolab, Phys. Rev. Lett. **101**, 015003 (2008).
[57]C. Theiler, I. Furno, P. Ricci, A. Fasoli, B. Labit, S. H. Müller, and G. Plyushchev, Phys. Rev. Lett. **103**, 065001 (2009).
[58]M. V. Umansky, T. D. Rognlien, and X. Q. Xu, J. Nucl. Mater. **337–339**, 266 (2005).